Research article

Electroosmotic MHD ternary hybrid Jeffery nanofluid flow through a ciliated vertical channel with gyrotactic microorganisms: Entropy generation optimization

Nidhish K. Mishra [a], Parikshit Sharma [b], Bhupendra K. Sharma [b,*], Bandar Almohsen [c], Laura M. Pérez [d]

[a] *Department of Basic Science, College of Science and Theoretical Studies, Saudi Electronic University, Riyadh, 11673, Saudi Arabia*
[b] *Department of Mathematics, Birla Institute of Technology and Science, Pilani, India*
[c] *Department of Mathematics, College of Science, King Saud University, Riyadh, 11451, Saudi Arabia*
[d] *Departamento de Física, FACI, Universidad de Tarapacá, Casilla 7D, Arica, 1000000, Chile*

ABSTRACT

In this study, the computational analysis of entropy generation optimization for synthetic cilia regulated ternary hybrid Jeffery nanofluid (Ag–Au–TiO$_2$/PVA) flow through a peristaltic vertical channel with swimming motile Gyrotactic microorganisms is investigated. Understanding the intricate interaction of multiple physical phenomena in biomedical applications is essential for optimizing entropy generation and advancing microfluidic systems. The characteristics of nanofluid are explored for the electroosmotic MHD fluid flow in the presence of thermophoresis and Brownian motion, viscous dissipation, Ohmic heating and chemical reaction. Using the appropriate transformations, a set of ordinary differential equations are created from the governing partial differential equations. The resulting ODEs are numerically solved using the shooting technique using BVP5C in MATLAB after applying the long-wavelength and low Reynolds number approximation. The velocity, temperature, concentration, electroosmosis, and microorganism density profiles are analyzed graphically for different emerging parameters. Graphical investigation of engineering interest quantities like heat transfer rate, mass transfer rate, skin friction coefficient, and entropy generation optimization are also presented. It is observed that the rate of mass transfer increases for increasing thermophoretic parameter, while reverse effect is noted for Brownian motion parameter, Schmidt number, and chemical reaction number. The outcomes of present study can be pertinent in studying Cilia properties of respiratory tract, reproductive system, and brain ventricles.

1. Introduction

Nanofluids are a type of liquid that contains suspended nanoparticles with at least one dimension between 1 and 100 nm. The nanoparticles may be metal, non-metal, or a combination of both and are typically disseminated in a base liquid like oil, water, or ethylene glycol. With an emphasis on applications for renewable energy, Li et al. [1] examine entropy generation in a hybrid nanofluid with Marangoni convective flow. Gowda et al. [2] examine the 3-D non-Newtonian MHD flow caused by surface stretching and

---

Nomenclature

Subscripts

f	Fluid
hnf	Hybrid nanofluid
nf	Nanofluid
thnf	Ternary hybrid nanofluid

Symbols

c	Wave speed (m/s)
PVA	Polyvinyl alcohol
(X^*, Y^*)	Fixed frame (in cartesian coordinates)
$+H$	Upper Cilia wall (m)
(U^*, W^*)	Velocity of HNF in (X^*, Y^*) direction (m/s)
k^*	Absorption coefficient (m^{-1})
t	Time (s)
p	Pressure (Pa)
F	Time-average flow rate (m^3/s)
T	Temperature (K)
C	Concentration (kg/m^3)
N	Microorganism density (kg/m^3)
S	Stress tensor (Pa)
G	Non-uniform parameter
v	Kinematic viscosity (m^2/s)
z	Charge balance (C)
g	Gravitational acceleration (m/s^2)
B_0	Strength of magnetic field (T)
(T_0, T_1)	Temperature at walls (K)
(C_0, C_1)	Concentration at walls (kg/m^3)
(N_0, N_1)	Microorganism density at walls (kg/m^3)
k_1	Permeability of the porous channel (m$^{2)}$)
k_b	Boltzmann constant
D_B	Brownian motion coefficient (m^2/s)
D_T	Diffusion coefficient of Thermophoretic (m^2/s)
D_N	Diffusion coefficient of Microorganisms (m^2/s)
q_r	Thermal heat flux (W/m^2)
b	Chemotaxis constant (m^2/s)
W_c	Maximum cell swimming speed (m/s)
k_r	Chemical reaction constant (s^{-1})
E_x	Electrokinetic body force (N/m^3)
d	Channel half width (m)
$a_i(s)$	Wave amplitudes (m)
(u, w)	Velocity of HNF in (x, y) direction (m/s)
m_0	Bulk concentration (kg/m^3)
T_{ave}	Average temperature (K)
$-H$	Lower Cilia wall (m)
(x, y)	Wave frame (in cartesian coordinates)
L	Cilia length parameter (m)
$b_i(s)$	Physical parameters of geometry
e	Electronic charge (C)

Greeks

ρ_e	Electric charge density (C/m^3)
μ	Dynamic viscosity (kg/(ms))
σ	Electrical conductivity (S/m)
ρ	Density (kg/m^3)
β_t	Volumetric thermal coefficient (K^{-1})
λ_1	Ratio of relaxation to retardation times
β_c	Volumetric concentration coefficient (m^3/kg)
λ_2	Retardation time (s)

c_p	Specific heat (J/(kg K))
γ	Volumetric microorganism density coefficient (m^3/kg)
ρ_p	Density of nanoparticles (kg/m^3)
ρ_m	Density of microorganisms (kg/m^3)
τ	Effective heat capacity (J/(kg K)
ψ	Stream function (m^2/s)
λ	Wavelength (m)
δ	Wavenumber (m^{-1})
σ^*	Stefan - Boltzmann constant (W/(m^{2}K^4))
ε	Permittivity of medium (F/m)
ε_0	Permittivity of free space (F/m)
k	Thermal conductivity (W/m K)
ζ	Zeta potential (V)
$\dot{\gamma}$	Shear rate (s^{-1})

chemical interactions. Belo et al. [3] examine the effects of aggregations in magnetohydrodynamic CNT-water nanofluid convection occurring naturally. Madhukesh et al. [4] investigate the thermal behavior of permeable inclined cylinder/plate ternary hybrid nanofluid flow. Sarada et al. [5] analyze internal heat generation's effect on a water-based ternary hybrid nanofluid flow using a non-Fourier heat flux model. Jyothi et al. [6] research the impact of Stefan blowing effect on Casson nanofluid flow and heat transfer over a moving thin needle. Alhadhrami et al. [7] analyze how the nanofluid Glauert wall jet slip flow is affected by thermophoretic particle deposition. Wang et al. [8] investigate the impact of on nanofluid flow between a disc and the gap of a cone, radiation and aggregation of nanoparticles. Alsulami et al. [9] examine the modified Maxwell-Bruggeman and Krieger-Dougherty models for 3-D swirling flow of nanofluid that includes dynamics of nanoparticle aggregation. Alsulamiet al. [10] examine heat transmission in non-Newtonian nanofluid flow through porous media under local thermal non-equilibrium circumstances. Using a Buongiorno model, Alsulami et al. [11] investigate bioconvection in radiative Glauert wall nanofluid jet flow. A numerical examination of heat transfer processes in the flow of ferromagnetic hybrid nanofluid via a stretched cylinder is done by Sreenivasa et al. [12].

Unlike conventional fluids, nanofluids show enhanced heat conduction due to the improved thermal conductivity conferred by the nanoparticles dispersed within the fluid. Second-grade magnetic nanomaterial entropy creation was simulated by Jamshed et al. [13] in expanding surface flow with viscidity dissipative flux. Elboughdiri et al. [14] passive control strategy is suggested for simulating thermally increased Jeffery nanofluid flows close to an impermeable barrier that has been suctioned. Wang et al. [15] investigate hybrid nanoparticle suspension in MHD mixed convective Falkner-Skan flow for water thermal increase in a porous medium. MHD nanofluid flow in a Darcy-Forchheimer medium is numerically treated by Rasool et al. [16] while taking radiative heat and mass transport laws into account. Sharma et al. [17] has done comparative analysis for Newtonian and non-Newtonian base fluids explore the influence of solutes on the heat sensitivity of nanofluids. An EMHD dissipative stagnation point flow model is created by Elboughdiri et al. [18] for radiating copper-based ethylene glycol nanofluids. Maxwell nanofluids that are radiating are studied by Wakif et al. [19] in 2-D MHD mixed bioconvective flows close to a vertical surface that is being heated convectively. Rasool et al.'s [20] investigation of EMHD-driven nanofluid flow through convective Riga surface for submissive control of alumina nanoparticles in aquatic medium. Wakif et al.'s [21] analysis highlights the significance of heat generation variability that is exponentially decreasing on chemically reactive nanofluid flows that are exposed to a radial magnetic field.

The surface of almost every mammalian cell, including those in the kidneys, lungs, esophagus, and respiratory system, is covered in minute string-like structures called cilia. These structures, which have a regular pounding action, are present in many significant human traits and essential functioning components. Nanofluid synthetic cilia have many applications and are under research. Synthetic cilia mimic natural cilia, improving fluid-based systems and enabling new biomedical, environmental, and materials science applications. Sharma et al. [22] utilized analyzing micropolar blood flow having ternary hybrid nanofluid with reactions using Bayesian regularization networks, optimizing entropy generation in a comprehensive study. Sharma et al. [23] employed an artificial neural network approach to investigate Darcy-Forchheimer hybrid nanofluid flow over a rotating Riga disk with chemical reactions, providing insights into fluid dynamics using advanced computational techniques. Tripathi et al. [24] numerically simulated electroosmosis and double-diffusive convection during micropolar nanofluid peristaltic transport on an asymmetric microchannel. Nanofluids have several potential applications in various fields, like energy conversion [25], heat transfer [26], environmental engineering [27], materials science [28], biomedical engineering [29], and thermal management [30]. While nanofluids have several potential benefits and applications, there are also several challenges and limitations that must be addressed before they can be widely adopted and commercialized.

The problem of MHD nanofluid peristaltic transport in an inclined channel with a porous medium has a numerical solution given by Abd-Alla et al. [31]. Chamkha et al. [32] studied laminar MHD mixed convection flow with both symmetric and asymmetric wall heating conditions in a vertical channel. Chamkha et al. [33] investigate fully developed free convection of a micropolar fluid in a vertical channel. Heat transport in a horizontal channel and unstable two-fluid flow are analyzed by Umavathi et al. [34]. Unsteady MHD laminar fluid-particle flow and heat transport in circular pipelines and channels are studied by Chamkha [35]. The fully developed free-convective flow of viscous and micropolar fluids in a vertical channel is studied by Kumar et al. [36]. A thorough analysis of mixed convection of nanofluids in a variety of enclosure forms is given by Izadi et al. [37]. The effects of induced magnetic field having thermal radiation on the convection flow of a dissipative fluid are described by Kumar et al. [38]. The radiative MHD
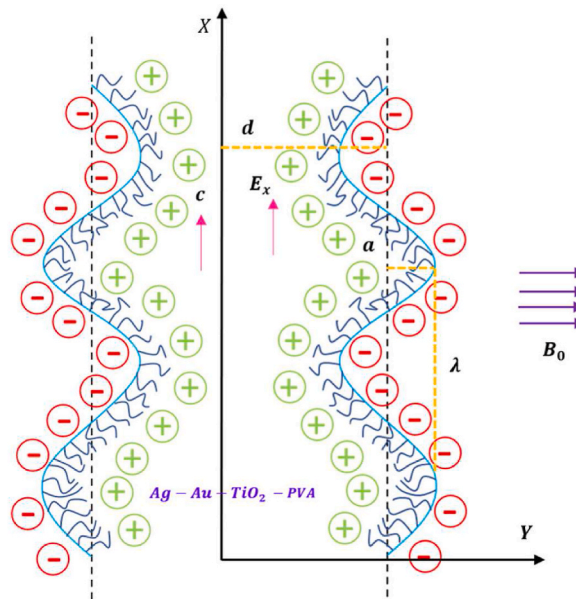
Fig. 1. Geometrical description of the Cilia regulated physical model.

Casson hybrid nanofluid flow across an infinite vertical porous surface is studied by Krishna et al. [39]. This study does not consider the ion slip and Hall effects. The neglection can be justified based on the specific conditions and scope of the research. For instance, studies done by Krishna et al. [40] and Krishna et al. [41] emphasize the significance of Hall and ion slip effects in rotating flows and specific biomedical applications. The current study does not involve rotating flows or similar biomedical contexts; hence these effects are less relevant here. Additionally, research done by Krishna et al. [42] and Chamkha et al. [43] focus on Hall effects in specific flow geometries, such as squeezing flows and vertical plates in thermally stratified porous media. The study under consideration does not involve such geometries or focuses on different physical phenomena.

Considering the preceding insightful literature review, the authors believe that there is no published research work on cilia regulated ternary hybrid nanofluid (Ag–Au–TiO$_2$ with PVA as the base fluid) with the effects of electroosmotic MHD, Joule heating, viscous dissipation, thermophoresis, Brownian motion, thermal radiation and chemical reaction, and entropy generation in a vertical channel. In this regard, a theoretical investigation is conducted to examine the mathematical characteristics of a study concerning the metachronal waves generated by the continuous beating of cilia in a vertical channel containing a nanofluid consisting of PVA as the base fluid and ternary hybrid nanofluid. This study introduces a novel paradigm by synergizing electroosmotic MHD effects, ternary hybrid Jeffery nanofluids, and gyrotactic microorganisms in ciliated vertical channels. The unprecedented entropy generation optimization potential of this intricate system promises advancements in energy efficiency and bio transport understanding. The introduction of new nanoparticles introduces a dynamic shift in the fundamental equations governing fluid flow and heat transfer. These nanoparticles, when integrated into the ternary hybrid Jeffery nanofluid, interact with the complex interplay of electroosmotic and magnetohydrodynamic effects. The main objective of the present research is to examine the effects of heat transfer coefficient, entropy generation, Bejan number, and microorganisms on flow characteristics. The study of electroosmosis, MHD, and cilia-induced flow in a Jeffery nanofluid helps to understand the transport and manipulation of gyrotactic microorganisms in fluid flows. These effects can be leveraged to control the behavior of microorganisms in applications like bioreactors and water treatment. The concentration and type of nanoparticles in the Jeffery nanofluid impact its viscosity, thermal conductivity, and other properties, influencing fluid flow and microorganism movement. More nanoparticles generally lead to higher viscosity, affecting the flow and microorganism motion. Cilia-induced flow results from the coordinated beating of cilia, hair-like structures on cell surfaces, creating a directed fluid flow. This

Table 1
Thermo-physical properties of ternary hybrid nanofluid.

Properties	Notation	Nanoparticles			Base fluid
		Ag	Au	TiO$_2$	PVA
Specific heat (J/kg K)	C_p	235	128	6012	2000
Density (kg/m3)	ρ	10500	19300	4175	1020
Thermal conductivity (W/m K)	k	429	328	8.4	0.2

mechanism plays a vital role in physiological processes such as mucus transport in respiratory systems and egg transport in reproductive tracts. In microfluidic devices and bioreactors, it can enhance fluid mixing, nutrient distribution, and control of microorganisms.

The current paper is organized as follows: formulation of the mathematical model is presented in Section 2, numerical implication is introduced in Section 3, validation of results is provided in Section 4, Results with necessary discussion is presented in section 5, and conclusions with applications are given in Section 6.

2. Problem formulation

Considered a two dimensional symmetric laminar viscous incompressible, thermally and electrically conducting $Ag - Au - TiO_2 - PVA$ ternary hybrid Jeffery nanofluid passing through a vertical channel. Cartesian coordinates are considered, and the flow is assumed two-dimensional peristaltic flow. The medium between the Cilia walls is assumed porous, having k_1 as the permeability constant. The medium contains microorganisms around the Cilia walls, having a density ρ_m. An external uniform magnetic field of strength B_0 is applied perpendicular to the flow. It is assumed that inner Cilia walls are covered with positive electric charges, and the outer walls are covered with negative electric charges. The flow is considered under the influence of Ohmic heating and viscous dissipation. The physical model of the problem to be studied is shown in Fig. 1. The Jeffery fluid is a specific non-Newtonian fluid model that incorporates both the Rivlin-Ericksen tensor and the Cauchy stress tensor. The Jeffery fluid model is often used to describe the behavior of viscoelastic fluids, such as those that exhibit shear-thinning or shear-thickening properties. In the Jeffery fluid model, the Rivlin-Ericksen tensor is used to describe the material's response to deformation, and the Cauchy stress tensor represents the stress distribution within the fluid. These tensors play a crucial role in characterizing the complex behavior of the fluid under different flow conditions. The Jeffrey fluid constitutive equation is given by Ref. [31]:

$$T = -p\mathbf{I} + S,$$

$$S = \frac{\mu_f}{1 + \lambda_1}\left(\dot{\gamma} + \lambda_2^* \frac{d\dot{\gamma}}{dt^*}\right)$$

The variables T, S, $\dot{\gamma}$, λ_1 (relaxation to retardation time ratio), λ_2^* (retardation time), and μ_f (viscosity) represent the Cauchy stress tensor, extra-stress tensor, and first Rivlin-Erickson tensor, respectively.

Eqs. (1) and (2) governs the top and lower Ciliated walls [32]:

$$+H = d + (X^* - ct^*)G + L\left\{a_1 \sin\left[\frac{b_1}{\lambda}(X^* - ct^*)\right] + a_2 \sin\left[\frac{b_2}{\lambda}(X^* - ct^*)\right] + a_3 \sin\left[\frac{b_3}{\lambda}(X^* - ct^*)\right]\right\}, \tag{1}$$

$$-H = -d - (X^* - ct^*)G - L\left\{a_1 \sin\left[\frac{b_1}{\lambda}(X^* - ct^*)\right] + a_2 \sin\left[\frac{b_2}{\lambda}(X^* - ct^*)\right] + a_3 \sin\left[\frac{b_3}{\lambda}(X^* - ct^*)\right]\right\} \tag{2}$$

The diverging regime is denoted by $G > 0$ and the convergence regime by the non-uniform parameter $G < 0$. The requirement that must be met for both Cilia walls is as follows: $d < a_1 + a_2 + a_3$. Under the above stated assumptions, the governing equations of this fluid are expressed as follows (Eq. (3) to Eq. (9)) [44–50]:

2.1. Continuity equation

$$\frac{\partial U^*}{\partial X^*} + \frac{\partial W^*}{\partial Y^*} = 0 \tag{3}$$

2.2. Momentum Equations

$$\rho_{thnf}\left[\frac{\partial U^*}{\partial t^*} + U^*\frac{\partial U^*}{\partial X^*} + W^*\frac{\partial U^*}{\partial Y^*}\right] = -\frac{\partial P^*}{\partial X^*} + g\beta_t(1 - C_0)(T^* - T_0) - (\rho_p - \rho_f)g\beta_c(C^* - C_0) - (\rho_m - \rho_f)g\gamma(N^* - N_0) - \sigma_{thnf}B_0^2 U^* + \frac{\partial S_{X^*X^*}^*}{\partial X^*}$$

$$- \frac{\mu_{thnf}}{k_1}U^* + \rho_e E_x + \frac{\partial S_{X^*Y^*}^*}{\partial Y^*} \tag{4}$$

$$\rho_{thnf}\left[\frac{\partial W^*}{\partial t^*} + U^*\frac{\partial W^*}{\partial X^*} + W^*\frac{\partial W^*}{\partial Y^*}\right] = -\frac{\partial P^*}{\partial Y^*} + \frac{\partial S_{Y^*Y^*}^*}{\partial Y^*} - \frac{\mu_{thnf}}{k_1}W^* + \frac{\partial S_{X^*Y^*}^*}{\partial X^*} \tag{5}$$

2.3. Energy equation

$$(\rho c_p)_{thnf}\left[\frac{\partial T^*}{\partial t^*}+U^*\frac{\partial T^*}{\partial X^*}+W^*\frac{\partial T^*}{\partial Y^*}\right]=k_{thnf}\left(\frac{\partial^2 T^*}{\partial X^{*2}}+\frac{\partial^2 T^*}{\partial Y^{*2}}\right)+\left[S^*_{X^*Y^*}\left(\frac{\partial U^*}{\partial Y^*}+\frac{\partial W^*}{\partial X^*}\right)+S^*_{Y^*Y^*}\frac{\partial W^*}{\partial X^*}+S^*_{X^*X^*}\frac{\partial U^*}{\partial X^*}\right]$$

$$+\tau(\rho c_p)_{thnf}\left[D_B\left(\frac{\partial T^*}{\partial X^*}\frac{\partial C^*}{\partial X^*}+\frac{\partial T^*}{\partial Y^*}\frac{\partial C^*}{\partial Y^*}\right)+\frac{D_T}{T_0}\left\{\left(\frac{\partial T^*}{\partial X^*}\right)^2+\left(\frac{\partial T^*}{\partial Y^*}\right)^2\right\}\right]+\sigma_{thnf}B_0^2 U^{*2}+\frac{\partial q_r}{\partial X^*}+\frac{\partial q_r}{\partial Y^*}$$

(6)

2.4. Concentration equation

$$\frac{\partial C^*}{\partial t^*}+U^*\frac{\partial C^*}{\partial X^*}+W^*\frac{\partial C^*}{\partial Y^*}=D_B\left(\frac{\partial^2 C^*}{\partial X^{*2}}+\frac{\partial^2 C^*}{\partial Y^{*2}}\right)+\frac{D_T}{T_0}\left(\frac{\partial^2 T^*}{\partial X^{*2}}+\frac{\partial^2 T^*}{\partial Y^{*2}}\right)-k_r^2(C^*-C_0)$$

(7)

2.5. Microorganisms Equation

$$\frac{\partial N^*}{\partial t^*}+U^*\frac{\partial N^*}{\partial X^*}+W^*\frac{\partial N^*}{\partial Y^*}=D_N\left(\frac{\partial^2 N^*}{\partial X^{*2}}+\frac{\partial^2 N^*}{\partial Y^{*2}}\right)-\frac{bW_c}{(C_1-C_0)}\left[\frac{\partial}{\partial X^*}\left(N^*\frac{\partial C^*}{\partial X^*}\right)+\frac{\partial}{\partial Y^*}\left(N^*\frac{\partial C^*}{\partial Y^*}\right)\right]$$

(8)

2.6. Poisson-Boltzmann equation

$$\frac{\partial^2\varphi^*}{\partial X^{*2}}+\frac{\partial^2\varphi^*}{\partial Y^{*2}}=-\frac{\rho_e}{\varepsilon\varepsilon_0}$$

(9)

Where, ρ_{thnf} is the density, σ_{thnf} is the electrical conductivity, μ_{thnf} is the dynamic viscosity, k_{thnf} is the thermal conductivity, and $(C_p)_{thnf}$ is the specific heat of the ternary hybrid nanofluid, respectively. The system of governing equations describes the hybrid nanofluid flow through a ciliated vertical channel with gyrotactic microorganisms. The continuity equation ensures the conservation of mass by balancing the flow velocities across the channel cross-section. In momentum equation, the fourth, fifth, and sixth terms of RHS represent the effects of buoyancy due to the temperature and concentration variations. Seventh term due to the magnetic field. Eighth term represents the porous medium, and the last term shows the electroosmosis effect. In energy equation, the second term of RHS represents the viscous dissipation. The third term represents the Brownian motion effect. The fourth term shows the thermophoresis effect. Fifth term comes for the Joule heating. The last terms show thermal radiation. In concentration equation, the first term from RHS shows the Brownian motion. The second term shows the thermophoresis effect. Last term represents the rates of chemical reaction. In microorganisms' equation, the first equation shows the microorganisms diffusion effect, and the second term shows represents the Chemotaxis effect. The Poisson-Boltzmann equation characterizes the electrostatic potential distribution within the nanofluid due to charged nanoparticles. The importance of the above equations in the study is discussed below:

a) **Continuity Equation** (3): Describes the conservation of mass in the fluid flow, accounting for variations in fluid density.
b) **Momentum Equations** (4) and (5): These equations capture the balance of forces that govern fluid motion, considering pressure, viscous effects, electromagnetic forces, and body forces.
c) **Energy Equation** (6): Represents the energy conservation in the system, incorporating heat conduction, fluid work, and the effects of electromagnetic fields.
d) **Concentration Equation** (7): Portrays the transport of particles or substances within the fluid, considering diffusion and convection.
e) **Microorganisms Equation** (8): Models the dynamics of gyrotactic microorganisms in the flow, accounting for their transport and interaction with the fluid.
f) **Poisson-Boltzmann Equation** (9): This equation describes the electrostatic potential and distribution of ions in a fluid, considering the influence of charges and their interactions.

The thermophysical characteristics of the current ternary hybrid nanofluid are presented in Table 1, and their mathematical expressions are defined by Eq. (10) [51]:

$$\frac{\mu_{thnf}}{\mu_f} = \left[\left(1 - \varphi_{Ag}\right)\left(1 - \varphi_{TiO_2}\right)\left(1 - \varphi_{Au}\right) \right]^{-2.5},$$

$$\frac{\rho_{thnf}}{\rho_f} = \left(1 - \varphi_{Ag}\right)\left[\left(1 - \varphi_{TiO_2}\right)\left\{ \left(1 - \varphi_{Au}\right) + \varphi_{Au}\frac{\rho_{Au}}{\rho_f} \right\} + \varphi_{TiO_2}\frac{\rho_{TiO_2}}{\rho_f} \right] + \varphi_{Ag}\frac{\rho_{Ag}}{\rho_f},$$

$$\frac{(\rho C_p)_{thnf}}{(\rho C_p)_f} = \left(1 - \varphi_{Ag}\right)\left[\left(1 - \varphi_{TiO_2}\right)\left\{ \left(1 - \varphi_{Au}\right) + \varphi_{Au}\frac{(\rho C_p)_{Au}}{(\rho C_p)_f} \right\} + \varphi_{TiO_2}\frac{(\rho C_p)_{TiO_2}}{(\rho C_p)_f} \right] + \varphi_{Ag}\frac{(\rho C_p)_{Ag}}{(\rho C_p)_f},$$

$$\frac{\sigma_{thnf}}{\sigma_{hnf}} = \left[\frac{\sigma_{Au} + 2\sigma_{hnf} - 2\varphi_{Au}\left(\sigma_{hnf} - \sigma_{Au}\right)}{\sigma_{Au} + 2\sigma_{hnf} + \varphi_{Au}\left(\sigma_{hnf} - \sigma_{Au}\right)} \right],$$

$$\frac{\sigma_{hnf}}{\sigma_{nf}} = \left[\frac{\sigma_{TiO_2} + 2\sigma_{nf} - 2\varphi_{TiO_2}\left(\sigma_{nf} - \sigma_{TiO_2}\right)}{\sigma_{TiO_2} + 2\sigma_{nf} + \varphi_{TiO_2}\left(\sigma_{nf} - \sigma_{TiO_2}\right)} \right],$$

$$\frac{\sigma_{nf}}{\sigma_f} = \left[\frac{\sigma_{Ag} + 2\sigma_f - 2\varphi_{Ag}\left(\sigma_f - \sigma_{Ag}\right)}{\sigma_{Ag} + 2\sigma_f + \varphi_{Ag}\left(\sigma_f - \sigma_{Ag}\right)} \right],$$

$$\frac{k_{thnf}}{k_{hnf}} = \left[\frac{k_{Au} + 2k_{Au} - 2\varphi_{Au}\left(k_{hnf} - k_{Au}\right)}{k_{Au} + 2k_{Au} + \varphi_{Au}\left(k_{hnf} - k_{Au}\right)} \right],$$

$$\frac{k_{hnf}}{k_{nf}} = \left[\frac{k_{TiO_2} + 2k_{nf} - 2\varphi_{TiO_2}\left(k_{nf} - k_{TiO_2}\right)}{k_{TiO_2} + 2k_{nf} + \varphi_{TiO_2}\left(k_{nf} - k_{TiO_2}\right)} \right],$$

$$\frac{k_{nf}}{k_f} = \left[\frac{k_{Ag} + 2k_f - 2\varphi_{Ag}\left(k_f - k_{Ag}\right)}{k_{Ag} + 2k_f + \varphi_{Ag}\left(k_f - k_{Ag}\right)} \right],$$

$$\varphi = \varphi_{Au} + \varphi_{TiO_2} + \varphi_{Ag}$$

(10)

In order to change the fluid flow problem from fixed frame—a time-dependent state—to wave frame—a time-independent state—the following transformations are applied:

$$X^* = x^* - ct^*, Y^* = y^*, U^* = u^* + c, W^* = w^*, P^*(X^*, Y^*, t^*) = p(x^*, y^*), T^* = T,$$
$$C^* = C, N^* = N$$

(11)

Now, to convert the dimensional PDEs into dimensionless PDEs, the following transformations are used:

$$x = \frac{x^*}{\lambda}, y = \frac{y^*}{d}, u = \frac{u^*}{c}, w = \frac{w^*}{c}, t = \frac{ct^*}{\lambda}, h = \frac{H}{d}, \delta = \frac{d}{\lambda}, p = \frac{d^2 p^*}{c\lambda\mu_f}, \lambda_2^* = \frac{c\lambda_2}{d}, S = \frac{S^* d}{c\mu_f},$$

$$r_i = \frac{a_i}{d}, q_i = \frac{b_i}{\lambda}, \psi = \frac{\psi^*}{cd}, \varphi = \frac{\varphi*}{\zeta}, \theta = \frac{T^* - T_0}{T_1 - T_0}, \Theta = \frac{C^* - C_0}{C_1 - C_0}, \chi = \frac{N^* - N_0}{N_1 - N_0}, \Omega = \frac{T_1 - T_0}{T_0}, \Pi = \frac{C_1 - C_0}{C_0}, \Gamma = \frac{N_0}{N_1 - N_0}$$

(12)

Where p is the pressure, φ is the electroosmotic potential, θ is the dimensionless temperature, Θ is the dimensionless concentration, χ is the dimensionless microorganism density, Π is the concentration ratio, Ω is the temperature ratio, and Γ is the microorganism density ratio. Using Rosseland estimation, q_r is expressed as follows [52]:

$$q_r = -\frac{4}{3}\frac{\sigma^*}{k^*}\nabla T^{*4}$$

The term T^{*4} can be represented as a linear temperature function in the Taylor series about T_0 and by ignoring the higher expressions and assuming that the temperature diffusion inside the flow is sufficiently modest, we obtain:

$$T^{*4} \approx -3T_0^4 + 4T^* T_0^3$$

After solving the Nernst-Planck equation and using the long wavelength, low Reynolds number, and low zeta potential, the electric charge density ρ_e is defined as [53]:

$$\rho_e = -\frac{2m_0(ez)^2\varphi^*}{k_b T_{ave}}$$

After using the transformations defined by equations 11 and 12, the governing equations (4)–(9) reduced as follows:

$$A_1 Re\delta\left[(1+u)\frac{\partial u}{\partial x} + \frac{w}{\delta}\frac{\partial u}{\partial y} \right] = -\frac{\partial p}{\partial x} + \delta\frac{\partial S_{xx}}{\partial x} + \frac{\partial S_{xy}}{\partial y} + A_1 Gr\theta - Gc\Theta - Rb\chi - \left(A_3 M^2 + \frac{A_2}{Da} \right)(1+u) + U_{HS}K^2\varphi$$

(13)

$$A_1 Re\delta^2\left[(1+u)\frac{\partial w}{\partial x} + \frac{w}{\delta}\frac{\partial w}{\partial y} \right] = -\frac{\partial p}{\partial y} + \delta^2\frac{\partial S_{xy}}{\partial x} + \delta\frac{\partial S_{yy}}{\partial y} - A_2\delta\frac{w}{Da}$$

(14)

$$A_4 Re\delta\left[(1+u)\frac{\partial\theta}{\partial x}+\frac{w}{\delta}\frac{\partial\theta}{\partial y}\right]=\frac{A_5+Rd}{Pr}\left(\delta^2\frac{\partial^2\theta}{\partial x^2}+\frac{\partial^2\theta}{\partial y^2}\right)+Ec\left[\delta S_{xx}\frac{\partial u}{\partial x}+S_{xx}\left(\frac{\partial u}{\partial y}+\delta\frac{\partial w}{\partial x}\right)+\delta S_{yy}\frac{\partial w}{\partial y}+M^2(1+u)^2\right]+Nb\left(\delta^2\frac{\partial\theta}{\partial x}\frac{\partial\Theta}{\partial x}+\frac{\partial\theta}{\partial y}\frac{\partial\Theta}{\partial y}\right)$$
$$+Nt\left[\delta^2\left(\frac{\partial\theta}{\partial x}\right)^2+\left(\frac{\partial\theta}{\partial y}\right)^2\right],$$

$$(15)$$

$$ScRe\delta\left[(1+u)\frac{\partial\Theta}{\partial x}+\frac{w}{\delta}\frac{\partial\Theta}{\partial y}\right]=\left(\delta^2\frac{\partial^2\Theta}{\partial x^2}+\frac{\partial^2\Theta}{\partial y^2}\right)+\frac{Nt}{Nb}\left(\delta^2\frac{\partial^2\theta}{\partial x^2}+\frac{\partial^2\theta}{\partial y^2}\right)-Kr_1Sc\Theta \tag{16}$$

$$LbRe\delta\left[(1+u)\frac{\partial\chi}{\partial x}+\frac{w}{\delta}\frac{\partial\chi}{\partial y}\right]=\left(\delta^2\frac{\partial^2\chi}{\partial x^2}+\frac{\partial^2\chi}{\partial y^2}\right)-Pe\left[\delta^2\frac{\partial\chi}{\partial x}\frac{\partial\Theta}{\partial x}+\frac{\partial\chi}{\partial y}\frac{\partial\Theta}{\partial y}+(\Gamma+\chi)\left(\delta^2\frac{\partial^2\Theta}{\partial x^2}+\frac{\partial^2\Theta}{\partial y^2}\right)\right] \tag{17}$$

$$\delta^2\frac{\partial^2\varphi}{\partial x^2}+\frac{\partial^2\varphi}{\partial y^2}=K^2\varphi \tag{18}$$

Where, A_{1-4} symbolize the ratios of the thermophysical characteristics of ternary hybrid nanofluids to those of the base fluid and are described as:

$$A_1=\frac{\rho_{thnf}}{\rho_f},A_2=\frac{\mu_{thnf}}{\mu_f},A_3=\frac{\sigma_{thnf}}{\sigma_f},A_4=\frac{(\rho c_p)_{thnf}}{(\rho c_p)_f},A_5=\frac{k_{thnf}}{k_f}$$

The non-dimensional parameters included in Eqs. 13–18 are as follows:

Gr (Thermal Grashof number) $=\frac{\rho_f g\beta_t(1-C_0)(T-T_0)d^2}{\mu_f c}$, Gc (Solutal Grashof number) $=\frac{(\rho_p-\rho_f)g\beta_c(C^*-C_0)d^2}{\mu_f c}$, Rb (Rayeigh number) $=\frac{(\rho_m-\rho_f)g\gamma(N^*-N_0)d^2}{\mu_f c}$, Re (Reynolds number) $=\frac{cd}{v_f}$, M (Magnetic number) $=\sqrt{\frac{\sigma_f}{\mu_f}}B_0 d$, Da (Darcy number) $=\frac{k_1}{d^2}$, Ec (Eckert number) $=\frac{c^2}{(c_p)_f(T_1-T_0)}$, Rd (Radiation parameter) $=\frac{16}{3}\frac{\sigma^*T_0^3}{k^*k_f}$, Pr (Prandtl number) $=\frac{\mu_f(c_p)_f}{k_f}$, Nb (Brownian motion parameter) $=\frac{\tau D_B(C_1-C_0)}{v_f}$, Nt (Thermophoresis parameter) $=\frac{\tau D_T(T_1-T_0)}{T_0 v_f}$, K (Electroosmotic parameter) $=dze\sqrt{\frac{2m_0}{k_b T_{ave}\varepsilon\varepsilon_0}}$, U_{HS} (Helmholtz–Smoluchowski velocity) $=-\frac{E_x\varepsilon\varepsilon_0\zeta}{\mu_f c}$, Kr_1 (Chemical reaction parameter) $=\frac{k_r^2 d^2}{v_f}$, Br (Brinkman number) $=PrEc$, Le (Lewis number) $=\frac{k_f}{D_B C_0}$, Lb (Bio-convection Lewis number) $=\frac{v_f}{D_N}$, Pe (Peclet number) $=\frac{bW_c}{D_N}$, Sc (Schmidt number) $=\frac{v_f}{D_B}$.

The Thermal Grashof number (Gr) measures the significance of buoyancy forces due to temperature differences relative to viscous forces in the fluid, while the Solutal Grashof number (Gc) does the same for concentration differences. The Rayleigh number (Rb) combines the effects of both temperature and concentration differences. The Reynolds number (Re) quantifies the importance of inertial forces compared to viscous forces in fluid flow. The Magnetic number (M) represents the influence of an applied magnetic field on the flow. The Darcy number (Da) indicates the ease of fluid flow through a porous medium. The Eckert number (Ec) represents the ratio of kinetic energy to enthalpy differences, indicating the significance of viscous dissipation. The Radiation parameter (Rd) measures the importance of thermal radiation in heat transfer. The Prandtl number (Pr) indicates the relative effectiveness of momentum transport compared to heat transport in the fluid. The Brownian motion parameter (Nb) quantifies the influence of Brownian motion on nanoparticle motion, while the Thermophoresis parameter (Nt) measures the influence of temperature gradients on nanoparticle motion. The Electroosmotic parameter (K) measures the strength of electroosmotic flow induced by an electric field, and the Helmholtz–Smoluchowski velocity (U_{HS}) represents the velocity induced by electroosmosis. The Chemical reaction parameter (Kr_1) measures the significance of chemical reactions on fluid flow. The Brinkman number (Br) quantifies the significance of viscous heating in the energy equation. The Lewis number (Le) indicates the relative effectiveness of heat transport compared to mass transport, while the Bio-convection Lewis number (Lb) represents the relative effectiveness of nutrient transport compared to viscous dissipation. The Peclet number (Pe) measures the importance of convective transport relative to diffusive transport, and the Schmidt number (Sc) indicates the relative effectiveness of momentum transport compared to mass transport.

Now, we would use the stream function ψ and the velocity fields described below:

$$u=\frac{\partial\psi}{\partial y}\ and\ w=-\delta\frac{\partial\psi}{\partial x}$$

The components of stress are represented by the following form:

$$S_{xx}=\frac{2\delta}{1+\lambda_1}\left[1+\frac{\lambda_2 c\delta}{d}\left(\frac{\partial\psi}{\partial y}\frac{\partial}{\partial x}-\frac{\partial\psi}{\partial x}\frac{\partial}{\partial y}\right)\right]\frac{\partial}{\partial y}\left(\frac{\partial\psi}{\partial x}\right),$$

$$S_{xy}=\frac{1}{1+\lambda_1}\left[1+\frac{\lambda_2 c\delta}{d}\left(\frac{\partial\psi}{\partial y}\frac{\partial}{\partial x}-\frac{\partial\psi}{\partial x}\frac{\partial}{\partial y}\right)\right]\left(\frac{\partial^2\psi}{\partial y^2}-\delta\frac{\partial^2\psi}{\partial x^2}\right),$$

$$S_{yy}=\frac{2\delta}{1+\lambda_1}\left[1+\frac{\lambda_2 c\delta}{d}\left(\frac{\partial\psi}{\partial y}\frac{\partial}{\partial x}-\frac{\partial\psi}{\partial x}\frac{\partial}{\partial y}\right)\right]\frac{\partial}{\partial y}\left(\frac{\partial\psi}{\partial x}\right)$$

Eq. 13–18 becomes: by using the low Reynolds number $(Re \to 0)$ and long wavelength $(\lambda \to \infty \Rightarrow \delta \to 0)$ approximations to the stress components and dimensionless governing equations.

$$\frac{\partial p}{\partial x} = \left(A_2 + \frac{1}{1+\lambda_1}\right)\frac{\partial^3 \psi}{\partial y^3} + A_1 Gr\theta - Gc\Theta - Rb\chi - \left(A_3 M^2 + \frac{A_2}{Da}\right)\left(1 + \frac{\partial \psi}{\partial y}\right) + U_{HS}K^2\varphi \tag{19}$$

$$\frac{\partial p}{\partial y} = 0 \tag{20}$$

$$(A_5 + Rd)\frac{\partial^2 \theta}{\partial y^2} + Br\left[A_2\left(\frac{\partial^2 \psi}{\partial y^2}\right)^2 + M^2\left(1 + \frac{\partial \psi}{\partial y}\right)^2\right] + PrNb\frac{\partial \theta}{\partial y}\frac{\partial \Theta}{\partial y} + PrNt\left(\frac{\partial \theta}{\partial y}\right)^2 = 0 \tag{21}$$

$$\frac{\partial^2 \Theta}{\partial y^2} + \frac{Nt}{Nb}\frac{\partial^2 \theta}{\partial y^2} - Kr_1 Sc\Theta = 0 \tag{22}$$

$$\frac{\partial^2 \chi}{\partial y^2} - Pe\left[\frac{\partial \chi}{\partial y}\frac{\partial \Theta}{\partial y} + (\Gamma + \chi)\frac{\partial^2 \Theta}{\partial y^2}\right] = 0 \tag{23}$$

$$\frac{\partial^2 \varphi}{\partial y^2} = K^2\varphi \tag{24}$$

From Eq. (19), the pressure gradient w.r.t x is eliminated by cross-difference. The resulting governing equation is obtained as follows:

$$\left(A_2 + \frac{1}{1+\lambda_1}\right)\frac{\partial^4 \psi}{\partial y^4} - \left(A_3 M^2 + \frac{A_2}{Da}\right)\frac{\partial^2 \psi}{\partial y^2} + A_1 Gr\frac{\partial \theta}{\partial y} - Gc\frac{\partial \Theta}{\partial y} - Rb\frac{\partial \chi}{\partial y} + U_{HS}K^2\frac{\partial \varphi}{\partial y} = 0 \tag{25}$$

With the following boundary conditions mentioned in Eq. (26) [54]:

$$\begin{aligned}
\psi &= +\frac{F}{2}, \frac{\partial \psi}{\partial y} = \frac{1}{1 - L[r_1 q_1 \cos(q_1 x) + r_2 q_2 \cos(q_2 x) + r_3 q_3 \cos(q_3 x)]}, \theta = 0, \Theta = 0, \chi = 0, \varphi = \zeta_1, at\ y = -h \\
\psi &= -\frac{F}{2}, \frac{\partial \psi}{\partial y} = \frac{1}{1 - L[r_1 q_1 \cos(q_1 x) + r_2 q_2 \cos(q_2 x) + r_3 q_3 \cos(q_3 x)]}, \theta = 1, \Theta = 1, \chi = 1, \varphi = \zeta_2, at\ y = +h
\end{aligned} \tag{26}$$

The physical significances of the boundary conditions are:

1) **Stream Function:** The stream function's value is constant along the cilia walls, representing the absence of relative motion between the fluid and the solid surface. This condition ensures that the fluid adheres to the cilia walls, preventing slip and maintaining accurate flow patterns.
2) **Temperature:** The dimensionless temperature profile varying from 0 to 1 indicates a transition from a baseline temperature to a potentially higher temperature. This gradient reflects a controlled thermal environment that could impact fluid-cilia interactions and microorganism behavior, influencing transport processes and energy exchange.
3) **Concentration:** The dimensionless concentration profile shifting from 0 to 1 suggests a transition from lower to higher concentration levels. This represents a gradient conducive to effective substance transport, diffusion, or chemical reactions near the cilia walls, playing a role in biological processes and transport phenomena.
4) **Microorganism Concentration:** The dimensionless microorganism concentration profile changing from 0 to 1 signifies a controlled density variation. This gradient could influence the distribution, alignment, and interaction of microorganisms with the fluid, affecting their transport behavior and potential biological effects.
5) **Zeta Potential:** The variation of zeta potential along the walls indicates changing electrokinetic properties. Zeta potential influences particle mobility, aggregation, and adhesion. A gradient in zeta potential could influence the electrical interactions between microorganisms, nanoparticles, and the fluid, thereby affecting their movement and behavior.

2.7. Physical quantities of interests

Physical characteristics including the mass transfer rate, heat transfer rate, and shear stress coefficient are now being examined in this work. The following are the mathematical formulae for the skin friction coefficient, Sherwood number, and Nusselt number as in Eq. (27) [55,56]:

$$Nu = \frac{d(q_w + q_r)}{k_f(T_1 - T_0)}, C_f = \frac{\tau_u}{\rho_f c^2}, Sh = \frac{dm_w}{\rho_f D_B(C_1 - C_0)} \tag{27}$$

Where, $(q_w + q_r)$ is the heat flux, τ_u is the axial stress, and m_w is the mass flux and defined as in Eq. (28):

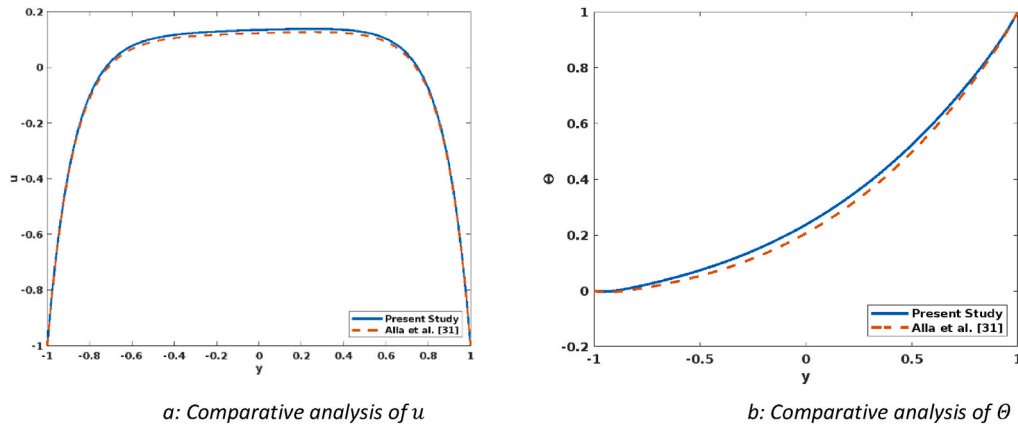a: Comparative analysis of u   b: Comparative analysis of Θ

Fig. 2. Comparative analysis.

$$q_w = -k_{thnf}\left(\frac{\partial T^*}{\partial Y^*}\right)_{Y^*=0}, q_r = -\frac{16T_0^3\sigma^*}{3k^*}\left(\frac{\partial T^*}{\partial Y^*}\right)_{Y^*=0}, \tau_u = \mu_{thnf}\left(\frac{\partial U^*}{\partial Y^*}\right)_{Y^*=0}, m_w = -\rho_f D_B\left(\frac{\partial C^*}{\partial Y^*}\right)_{Y^*=0} \tag{28}$$

In terms of the similarity variable, the skin friction coefficient, the Sherwood number and the Nusselt number are all stated as follows in their non-dimensional versions as in Eq. (29):

$$Nu = -(A_5 + Rd)\theta'(0), C_f Re = A_2 u'(0), Sh = -\Theta'(0) \tag{29}$$

2.8. Entropy generation

The development of entropy in a process caused by convection-radiation-based heat transfer, Ohmic heating, and viscous dissipation is defined mathematically by the second law of thermodynamics as Eq. (30) [57,58]:

$$S_{gen} = \frac{1}{T_0^2}\left[k_{thnf} + \frac{16\sigma^*(T_1 - T_0)^3}{3k^*}\right](\nabla T^*)^2 + \frac{\mu_{thnf}}{T_0}\left(\frac{\partial^2\psi^*}{\partial y^{*2}}\right)^2 + \frac{\mu_{thnf}}{T_0}\left(\frac{1}{1+\lambda_1}\right)\left(\frac{\partial^2\psi^*}{\partial y^{*2}}\right)^2 + \frac{\sigma_{thnf}B_0^2}{T_0}\left(c + \frac{\partial\psi^*}{\partial y^*}\right)^2 + \frac{D_B}{C_0}(\nabla C^*)^2 + \frac{D_B}{T_0}(\nabla T^* \nabla C^*) \tag{30}$$

The following Eq. (31) may be obtained using the total entropy generation number formula, lubrication approximations, and the characteristic entropy using Eqs. (11) and (12) in Eq. (30):

$$N_G = \underbrace{\left(A_5 + \frac{Rd}{PR}\right)\left(\frac{\partial\theta}{\partial y}\right)^2}_{N_T} + \underbrace{\frac{Br}{\Omega}\left(\frac{\partial^2\psi}{\partial y^2}\right)^2}_{N_V} + \underbrace{A_2\frac{Br}{\Omega}\left(\frac{1}{1+\lambda_1}\right)\left(\frac{\partial^2\psi}{\partial y^2}\right)^2}_{N_F} + \underbrace{A_3\frac{BrM^2}{\Omega}\left(1 + \frac{\partial\psi}{\partial y}\right)^2}_{N_J} + \underbrace{\left(\frac{\Pi}{\Omega}\frac{\partial\Theta}{\partial y}\right)^2 + \frac{\Pi}{\Omega Le}\left(\frac{\partial\theta}{\partial y}\frac{\partial\Theta}{\partial y}\right)}_{N_M} \tag{31}$$

Table 2
Various cases and values of parameters.

Parameter	Case-1	Case-2	Case-3
Gr	0.5	1.5	2.5
M	1	4	7
Da	0.01	0.03	0.05
U_{HS}	1	2	3
Pr	3	5	7
Br	0.5	0.6	0.7
Rd	0.6	0.8	1.0
F	0.1	0.2	0.3
Nb	0.5	0.6	0.7
Nt	0.5	0.6	0.7
Kr_1	1	6	12
Γ	0.1	0.5	1.0
Pe	0.1	0.2	0.3
Sc	1	5	10
ζ_1	0.020	0.025	0.030
K	2	3	4
φ_{Ag}	0.01	0.05	0.10
φ_{Au}	0.01	0.05	0.10

In this case, the irreversibility's N_J for ohmic heating, N_M for mass transfer, N_V for viscous, N_F for fluid friction, and N_T for thermal irreversibility are all present. The Bejan number, Be, indicates the ratio of irreversibility due to heat transfer to overall irreversibility induced. In mathematical notation, it is defined as in Eq. (32):

$$Be = \frac{\left(A_5 + \frac{Rd}{PR}\right)\left(\frac{\partial\theta}{\partial y}\right)^2}{\left(A_5 + \frac{Rd}{PR}\right)\left(\frac{\partial\theta}{\partial y}\right)^2 + \frac{Br}{\Omega}\left(\frac{\partial^2\psi}{\partial y^2}\right)^2 + A_2\frac{Br}{\Omega}\left(\frac{1}{1+\lambda_1}\right)\left(\frac{\partial^2\psi}{\partial y^2}\right)^2 + A_3\frac{BrM^2}{\Omega}\left(1+\frac{\partial\psi}{\partial y}\right)^2 + \left(\frac{\Pi}{\Omega}\frac{\partial\Theta}{\partial y}\right)^2 + \frac{\Pi}{\Omega Le}\left(\frac{\partial\theta}{\partial y}\frac{\partial\Theta}{\partial y}\right)} \quad (32)$$

3. Numerical solution

The Shooting procedure is a method for solving a boundary value problem (BVP) in computational analysis by transforming it into an initial value problem (IVP) of a first order differential equation. It involves locating solutions to the IVP for various initial conditions until a solution is found that also satisfies the BVP's boundary conditions. The differential equations 21–25 and the boundary conditions (26) are solved by convenient shooting method numerically. Initially, the higher-order differential equations are transformed into first-order equations using new transformations. The substitutions used for this are as follows in Eq. (33):

$$Y_1 = \psi, Y_2 = \frac{\partial\psi}{\partial y}, Y_3 = \frac{\partial^2\psi}{\partial y^2}, Y_4 = \frac{\partial^3\psi}{\partial y^3}, Y_5 = \theta, Y_6 = \frac{\partial\theta}{\partial y}, Y_7 = \Theta, Y_8 = \frac{\partial\Theta}{\partial y}, Y_9 = \chi, Y_{10} = \frac{\partial\chi}{\partial y}, Y_{11} = \varphi, Y_{12} = \frac{\partial\varphi}{\partial y}, Y_6' = \xi_1, Y_8' = \xi_2 \quad (33)$$

Ninefirst-orderdifferentialequationscomprisetheinitialvalueissuethatarisesfromthesesubstitutions

$$\left.\begin{aligned}
Y_1' &= Y_2, \\
Y_2' &= Y_3, \\
Y_3' &= Y_4, \\
Y_4' &= \frac{\left(A_3M^2 + \frac{A_2}{Da}\right)Y_3 - A_1GrY_6 + GcY_8 + RbY_{10} - U_{HS}K^2Y_{12}}{\left(A_2 + \frac{1}{1+\lambda_1}\right)}, \\
Y_5' &= Y_6, \\
Y_6' &= \frac{-Br\left[A_2(Y_3)^2 + M^2(1+Y_2)^2\right] - PrNbY_6Y_8 - PrNt(Y_6)^2}{(A_5 + Rd)}, \\
Y_7' &= Y_8, \\
Y_8' &= -\frac{Nt}{Nb}\xi_1 + Kr_1ScY_7, \\
Y_9' &= Y_{10}, \\
Y_{10}' &= Pe[Y_8Y_{10} + (\Gamma + Y_9)\xi_2], \\
Y_{11}' &= Y_{12}, \\
Y_{12}' &= K^2Y_{11}
\end{aligned}\right\} \quad (34)$$

With the following boundary conditions:

$$Y_1(-h) = \frac{Q}{2}; Y_2(-h) = -1; Y_5(-h) = 0; Y_7(-h) = 0; Y_9(-h) = 0; Y_{11}(-h) = \zeta_1; Y_1(+h) = -\frac{Q}{2}; Y_2(+h) = -1; Y_5(+h) = 1; Y_7(+h)$$
$$= 1; Y_9(+h) = 1; Y_{11}(+h) = +\zeta_2 \quad (35)$$

The numerical results for Eq. (34) with the boundary conditions of Eq. (35), obtained using MATLAB's BVP5C.

4. Validation of model

To validate the current methodology, the existing model is derived from a previously published study by Alla et al. [31] after removing the new terms considered in the current study. Fig. 2a and b represent the validation of the present model with Alla et al. [31] for u and Θ, respectively. Some terms in the set of governing differential equations are nullified and matched with their governing equations. From the figures, it is observed that the present study has good agreement with the earlier published work.

Table 3
References and ranges of parameters.

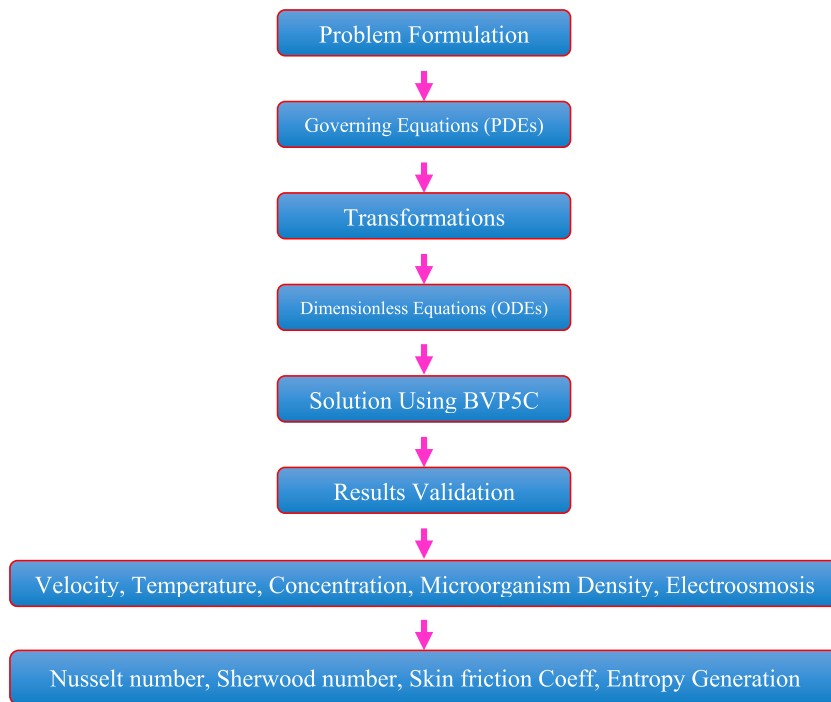| Parameter	Range	Default	References
Gr	[0–5]	0.5	[63]
Gc	[0–5]	0.5	[63]
Rb	[0–5]	0.5	[63]
M	[0–10]	2	[67]
Da	[0–1]	0.03	[64]
Pr	[0–20]	7.743	[61]
Br	[0–5]	0.5	[60]
Rd	[0–10]	0.5	[59]
K	[0–5]	2	[65]
U_{HS}	[0–5]	5	[65]
Nb	[0–0.5]	0.3	[66]
Nt	[0–0.5]	0.2	[66]
Kr_1	[0–15]	0.5	[67]
λ_1	[0–5]	1	[31]
Γ	[0–1]	1	[67]
Pe	[0–1]	0.3	[63]
Sc	[0–10]	0.3	[67]
ζ	[-1,1]	0.025	[49]
F	[0–1]	0.05	[49]
φ	[0–1]	0.1	[62]

Fig. 3. Model simulation.

5. Results and discussions

To get physical insight into the problem, a combined effect of viscous dissipation, Ohmic heating, uniform magnetic field, electroosmotic, thermophoresis, Brownian motion, thermal radiation, and chemical reaction is investigated in this section. Different graphs of velocity, temperature, concentration, electroosmosis, and microorganism density profiles are plotted for a combination of dimensionless parameters. The different cases and default values with range of parameters are shown in Table-2 and Table-3, respectively. Fig. 3 shows the simulation process of the current model.

5.1. Velocity profiles

Fig. 4 shows the axial velocity profiles for the effects of the thermal Grashof number, Darcy number, magnetic number, and
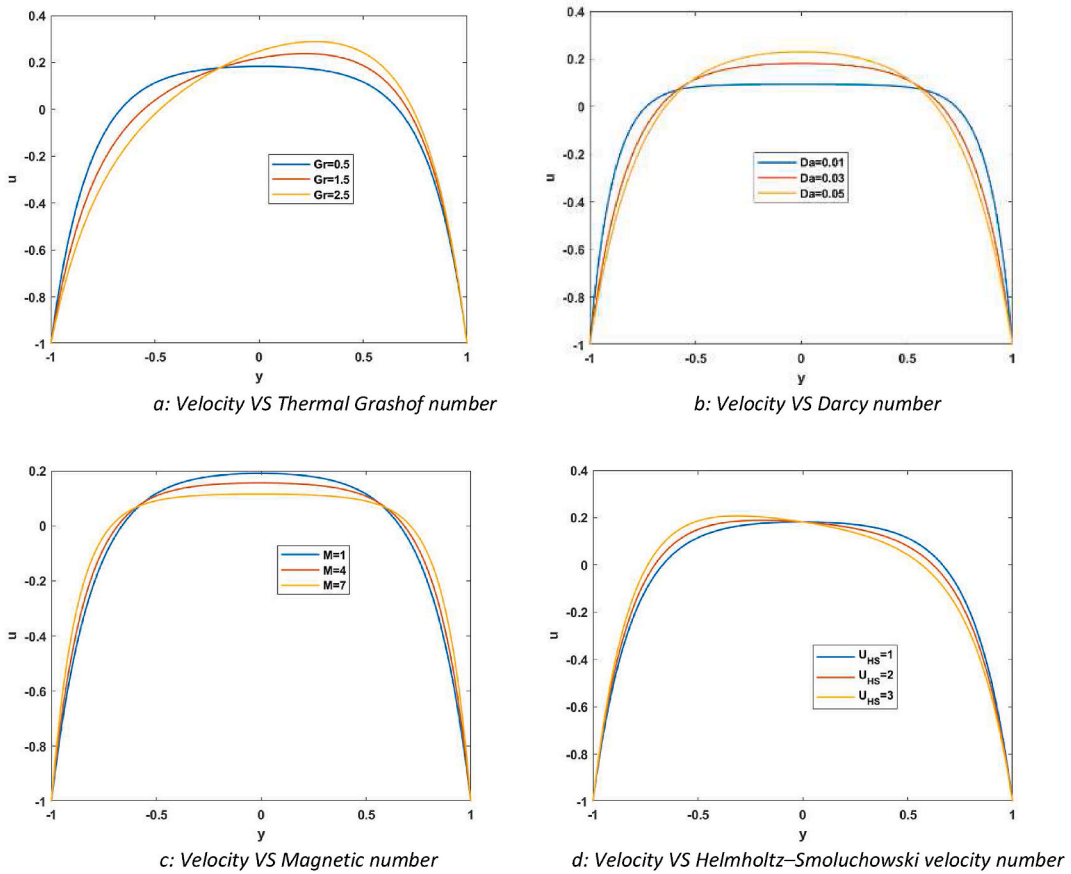
a: Velocity VS Thermal Grashof number

b: Velocity VS Darcy number

c: Velocity VS Magnetic number

d: Velocity VS Helmholtz–Smoluchowski velocity number

Fig. 4. Velocity profiles.

Helmholtz–Smoluchowski velocity number. Fig. 4a shows how increasing the thermal Grashof number (Gr) affects fluid velocity. On increasing Gr, the velocities decreased for the first half, around zero, then in the second half, it increased. Gr expresses the relationship between buoyancy and viscous forces. Gr values above one indicates that buoyant forces are stronger than viscous forces. With a higher Gr value, the temperature gradient rises, and the buoyancy contribution near the right wall becomes larger, increasing velocity there. In contrast, the opposite occurs near the left side wall. Fig. 4b shows the effect of Darcy number (Da) on velocity profiles. On increasing the Da, the velocity increases as higher Da implies more space for the nanofluid to circulate freely, hence a faster speed and recirculation. Fig. 4c reveals the effect of magnetic number (M) on the velocity. It is observed that increasing M reduces the velocity profiles. The applied magnetic field intensity increases when M increases, and Lorentz forces become more strongly resistive. The speed of nanoparticles is reduced because of the increased resistance to fluid flow caused by Lorentz forces. Fig. 4d communicates that increasing the Helmholtz–Smoluchowski number (U_{HS}) increases the velocity for the first half, then decreases for the second half. When U_{HS} is increased, viscoelastic effects are dampened, and the velocity increases dramatically close to the left wall, whereas the opposite is true for the right wall.

5.2. Temperature profiles

Fig. 5 exhibits the effect on temperature for magnetic number, Darcy number, Brinkman number, Radiation number, Average time flow rate number, and concentration of gold. Fig. 5a shows the temperature profiles for magnetic numbers (M). It is observed that by increasing the magnetic number, the temperature profiles increased drastically. The fluid's temperature is an increasing function of M. When M is boosted, Lorentz forces are amplified. As a result, more heat will be produced as more energy is lost to maintain the necessary fluid movement. Fig. 5b conveys the temperature profiles for Darcy number (Da). From the figure it is noticed that by increasing Da, the temperature of fluid increases. When Da grows, the porosity of the medium does as well, slowing the mobility of the liquid and increasing the frictional heating significantly. Fig. 5c gives us the temperature profiles for Brinkman number (Br). It shows that on increasing Br, the temperature profiles increase. Increases in Br increase the viscous force and, hence, the likelihood of a kinematic collision. As the Br value increases, the irreversibility of viscous dissipation becomes greater than that of heat transfer. The Br is the ratio of the heat lost or gained due to viscous dispersion and the heat supplied by molecules of the liquid. As a result, increased Br indicates that more heat is generated via viscous dispersion than is transmitted via molecular conduction. Fig. 5d indicates the effect
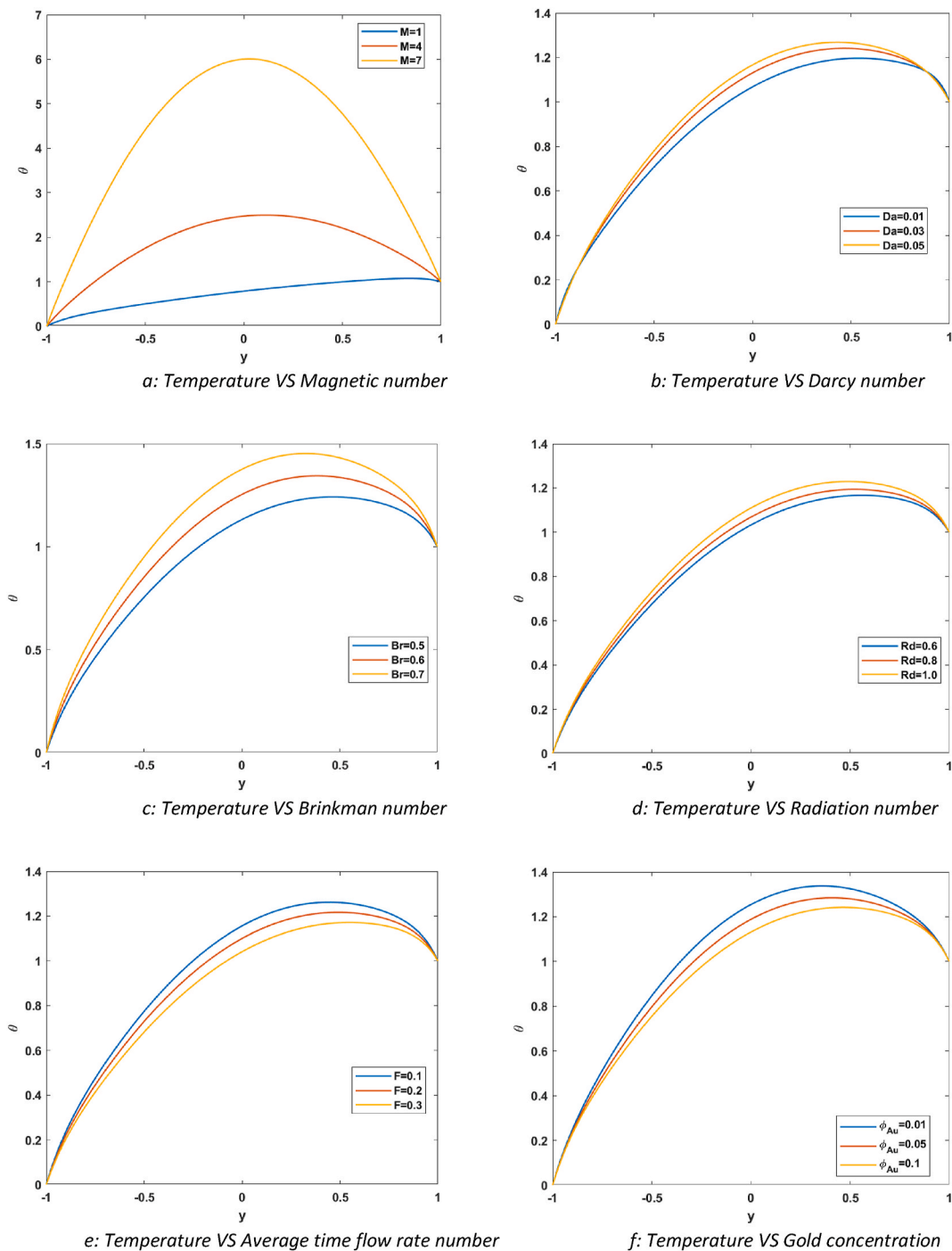
Fig. 5. Temperature profiles.

of radiation number (Rd) on the temperature profiles. As Rd increases, the temperature of fluid also rises. Increases in Rd lead to higher liquid temperatures and densities in their thermal boundary layers. This is because the nanofluids' temperature profile and thermal boundary layer width increase noticeably with an increase in Rd. Radiation emission is amplified using a more physically nuanced estimate of Rd, increasing the collision between fluid particles. Fig. 5e depicts the average time flow rate number (F) temperature profiles. It can be seen from the figure that on increasing F, the temperature of fluid decreases. Fig. 5f shows the effect of the concentration of gold on temperature. The temperature drops, on improving the concentration of gold by 1 %, 5 %, and 10 %.
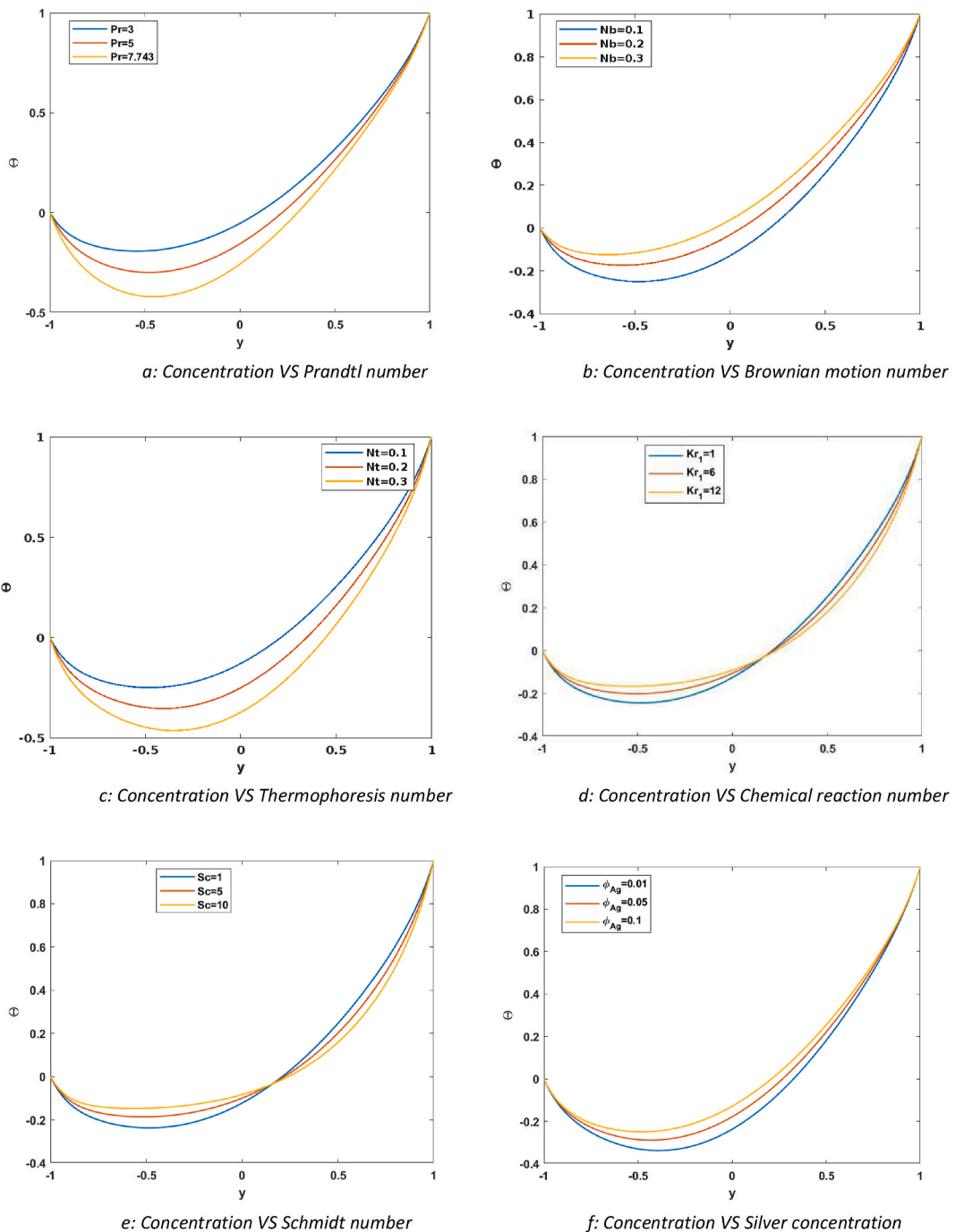
a: Concentration VS Prandtl number

b: Concentration VS Brownian motion number

c: Concentration VS Thermophoresis number

d: Concentration VS Chemical reaction number

e: Concentration VS Schmidt number

f: Concentration VS Silver concentration

Fig. 6. Concentration profiles.

5.3. Concentration profiles

Fig. 6 shows the effect on concentration profile for Prandtl number, Brownian morion number, thermophoresis number, chemical reaction number, Schmidt number, and concentration of silver nanoparticles. Fig. 6a reveals the concentration profiles for the different values of Prandtl number (Pr). It is noticed that by increasing Pr, the concentration profile drops. This is because Pr depends on the diffusivity and Higher Pr corresponds to weaker diffusivity, which tends to lower the concentration and thinner boundary layer thickness. Fig. 6b shows the fluid's concentration for Brownian motion number (Nb). On enhancing Nb, the concentration profiles increase. The Brownian motion refers to the random motion of nanoparticles in the base fluid. The rapid motion of the fluid's atoms or
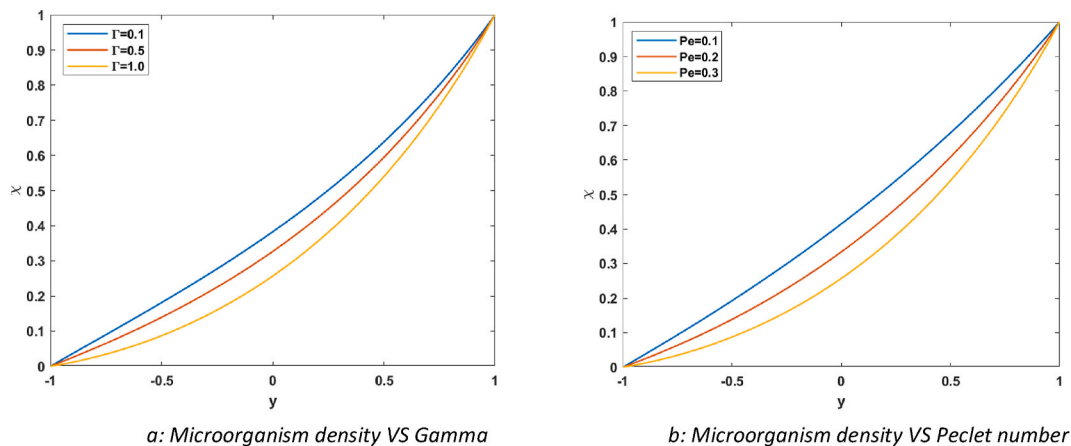
a: Microorganism density VS Gamma   b: Microorganism density VS Peclet number

Fig. 7. Microorganism density orofiles.

a: Electroosmosis VS ζ_1 b: Microorganism density VS Electroosmotic number
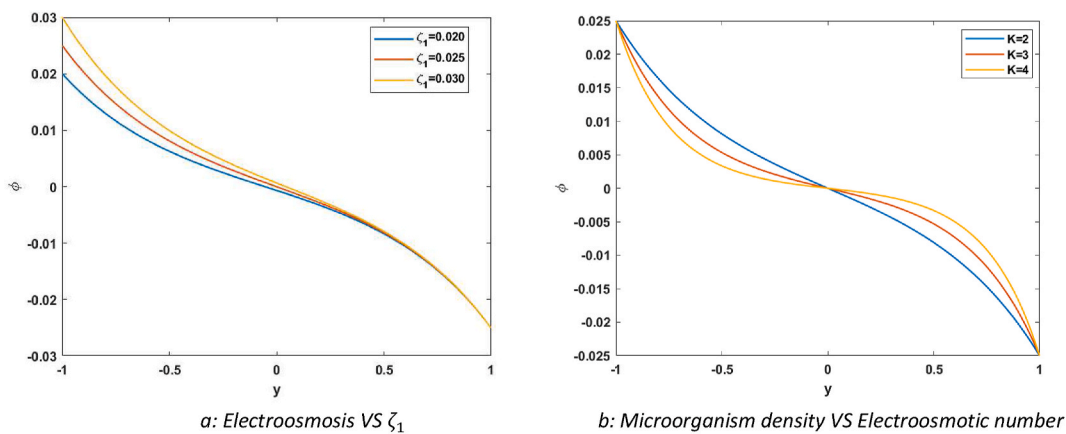
Fig. 8. Electroosmosis profiles.

molecules has a greater effect on Br. Brownian motion is proportional to the size of the particles involved, and particles often assemble into larger structures called agglomerates. As heavy particles experience negligible Brownian motion, Nb will have the lowest value. Hence, the concentration profiles become steeper as Nb values rise. Fig. 6c indicates the effect of the thermophoresis number (Nt) on fluid concentration. On increasing Nt, the concentration of the fluid decreases. This is because the concentration and boundary layer thicknesses are reduced due to the thermophoretic force exerted by the particles near the surface as Nt increases. The purpose of Fig. 6d is to show how the chemical reaction number (Kr_1) affects the concentration profiles. On increasing Kr_1, the concentration increases for the first half and then decreases for the second half. The expansion of Kr_1 near the right surface is considered to increase collisions between fluid particles, decreasing the concentration of the ternary hybrid nanofluid and thinning the boundary layer. However, the reverse trend holds on the left. Fig. 6e depicts the consequence of the Schmidt number (Sc) on the concentration profiles. On increasing Sc, the fluid's concentration increases on the left side and then decreases on the right side. Physically, as Sc rises, the molecule diffusivity falls. Sc is defined as the ratio between momentum and mass diffusivities. Thus, momentum diffusion will predominate for large Sc, as evidenced by increasing Sc leading to higher dynamic viscosity and lower density. Fig. 6f illustrates the effect of the concentration of silver on the fluid concentration. On increasing the silver concentration, the fluid concentration increases.

5.4. Microorganism density profiles

Fig. 7 shows the effect of the microorganism density ratio and Peclet number on the microorganism density. Fig. 7a shows the changes in microorganism density for microorganism density ratio (Γ). By increasing Γ, the microorganism density decreases. Γ is the ratio of the initial concentration at the wall to the change in concentration. Fig. 7b shows the changes in concentration profiles for Peclet number (Pe). Enhanced *Pe* decrease the microorganisms' density profile. This is because *Pe* decreases the diffusivity of the total number of microorganisms and their density profile within the boundary layer. *Pe* also increases the Brownian motion of nanoparticles in the base fluid.
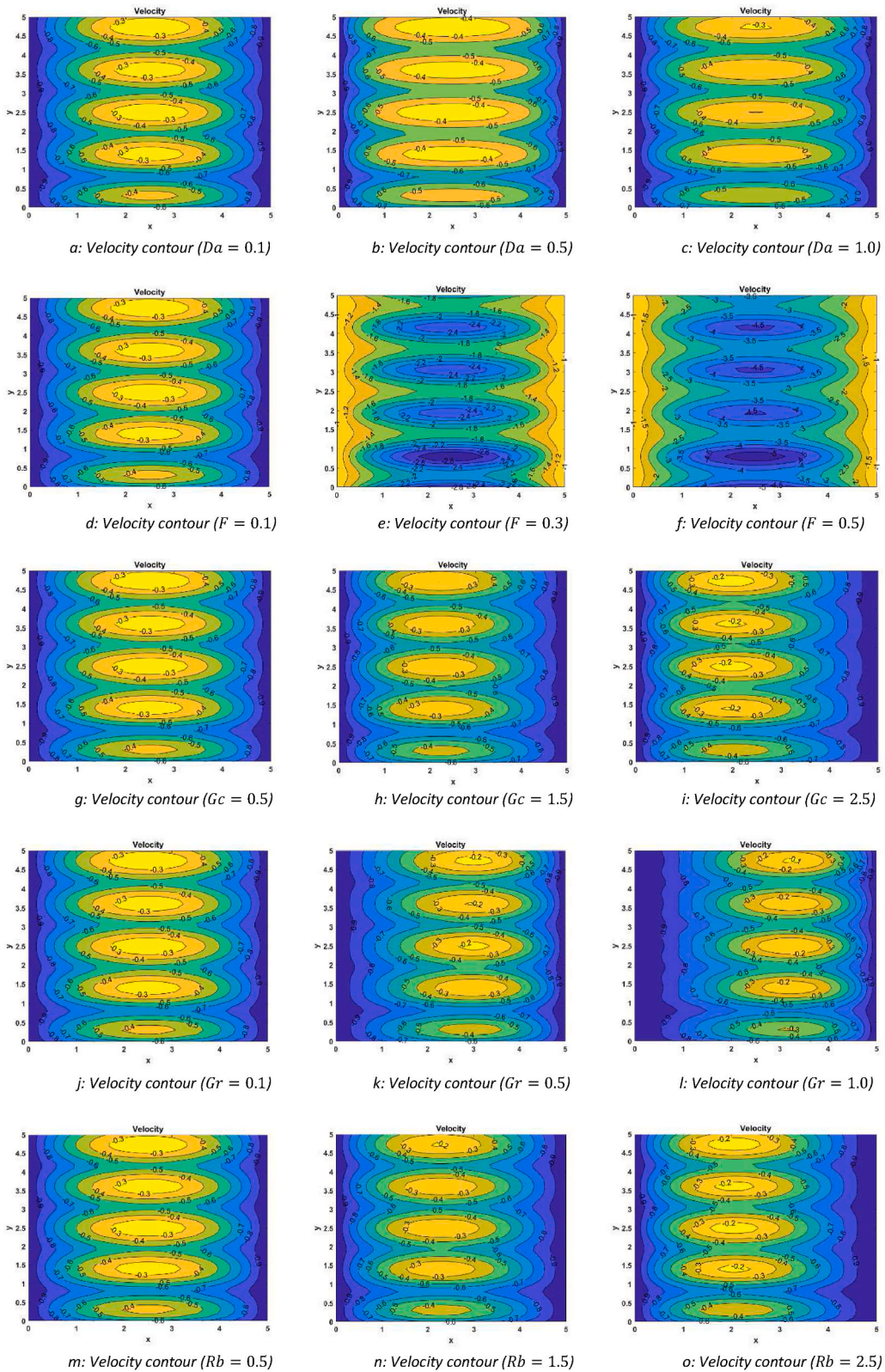
a: Velocity contour ($Da = 0.1$)

b: Velocity contour ($Da = 0.5$)

c: Velocity contour ($Da = 1.0$)

d: Velocity contour ($F = 0.1$)

e: Velocity contour ($F = 0.3$)

f: Velocity contour ($F = 0.5$)

g: Velocity contour ($Gc = 0.5$)

h: Velocity contour ($Gc = 1.5$)

i: Velocity contour ($Gc = 2.5$)

j: Velocity contour ($Gr = 0.1$)

k: Velocity contour ($Gr = 0.5$)

l: Velocity contour ($Gr = 1.0$)

m: Velocity contour ($Rb = 0.5$)

n: Velocity contour ($Rb = 1.5$)

o: Velocity contour ($Rb = 2.5$)

Fig. 9. Velocity contours.

m: Velocity contour (Rb = 0.5)

n: Velocity contour (Rb = 1.5)

o: Velocity contour (Rb = 2.5)

p: Velocity contour (M = 1.0)

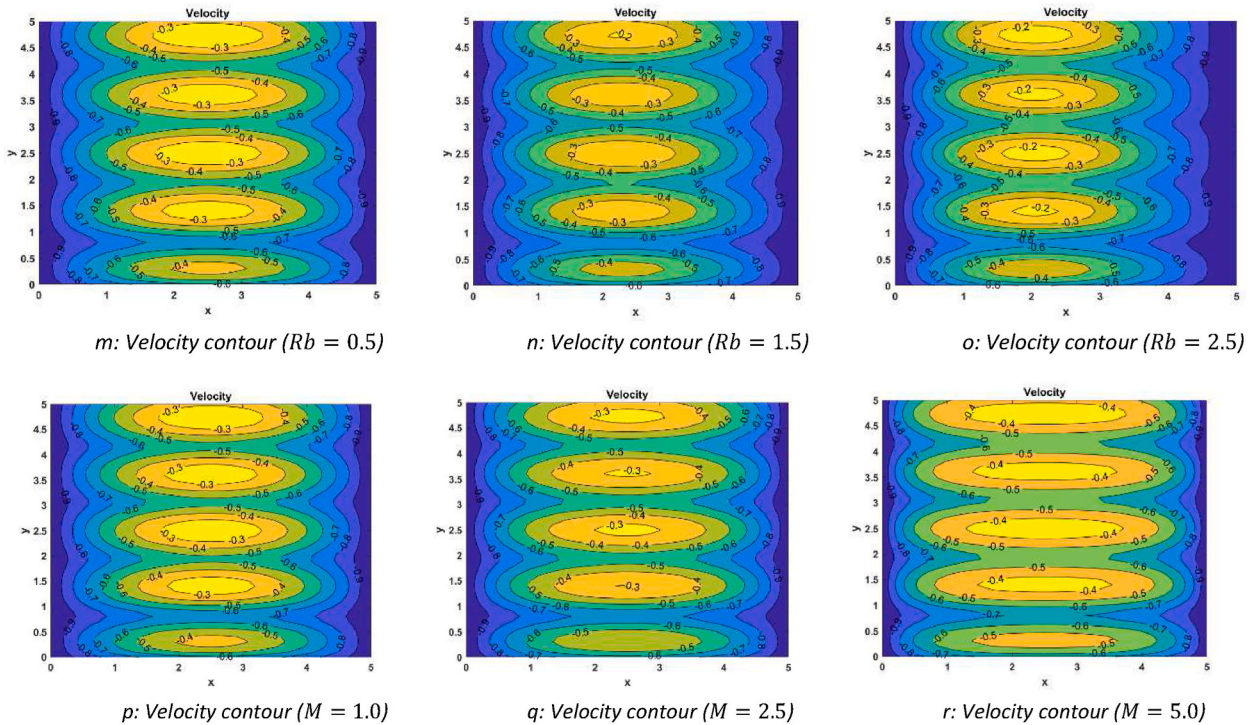q: Velocity contour (M = 2.5)

r: Velocity contour (M = 5.0)

Fig. 9. (continued).

5.5. Electroosmosis profiles

Fig. 8 illustrates the effect of zeta potential and electroosmotic number on the electroosmosis process. Fig. 8a shows the effect of the zeta potential of the left wall on electroosmosis. It shows that for enhanced zeta potential, the electroosmosis process becomes faster. Mathematically, the zeta potentials are used in the boundary condition in this model. Physically, the potential distribution is related to the strength of the electrical field. The stronger the zeta potential, the higher the concentration of ions adjacent to the channel wall and the more rapidly the potential improves. As a result, the electrical field intensity only dominates a tiny layer near the channel wall and increases as the zeta potential does. When the zeta potential is high enough, the electrical field strength dominates the thin layer at the interface. Fig. 8b shows the effect of the electroosmotic number (K) on electroosmosis. On enhancing K, the electroosmosis first decreased, and then it increased. This behavior is foreseen because an increase in Debye thickness triggers a thin electric double layer, leading to a significant increase in liquid flow at the pump's epicenter.

5.6. Velocity contours

Fig. 9 shows the velocity contours for six dimensionless numbers. On changing Da from 0.1 to 0.5, the bolus size decreases (Fig. 9a and b). The innermost yellow bolus is affected the most. On making $Da = 1.0$, the yellow bolus almost disappears (Fig. 9c). The boluses also spread horizontally. On increasing F, the inner boluses start disappearing. For F from 0.1 to 0.3, the inner yellow and orange boluses disappear (Fig. 6d and e), and a horizontal stretching is also seen. For $F = 0.5$, the inner boluses again disappear, and the outer layers start squeezing inside (Fig. 9f). For $Gc = 0.5$ to 1.5, the innermost yellow bolus disappeared, and a leftward flow shift happens (Fig. 9g and h). For $Gc = 2.5$, the inner boluses again appear. The yellow bolus again starts its formation (Fig. 9i). For Gr, from 0.1 to 0.5, the innermost bolus starts disappearing (Fig. 9j and k). For $Gr = 1.0$, the inner bolus got disappeared except for the top and bottom one (Fig. 9l). There is also a rightward shift of fluid flow is seen. For $Rb = 0.5$ to 1.5, the innermost bolus disappears, and a leftward shift happens (Fig. 9m and n). $Rb = 2.5$ shows the enhancement in the left shift and the formation of yellow bolus again (Fig. 9o). For $M = 1.0$ to $M = 2.5$, the inner yellow bolus size reduces (Fig. 9p and q). In the lowest part, it disappears, and the outer green layer forms the bolus. For $M = 5.0$, the yellow bolus stretches horizontally (Fig. 9r).

5.7. Temperature contours

Fig. 10 shows the temperature contours for different physical parameters. There are vertical ways of temperature formed for X and Y coordinates. Firstly, for $Br = 1.0$ to $Br = 2.0$, the amplitude of these waves increases drastically (Fig. 10a and b). There is also the formation of boluses toward the right waves and further for $Br = 10c$, the boluses disappear. The amplitude of waves remains almost unchanged (Fig. 10c). For $Rd = 3.0$ from 1.0, the wayes stretch a lot vertically, and the amplitude of these waves decreases a lot

(Fig. 10d and e). For $Rd = 5$, the waves almost take the form of straight lines. The amplitude becomes ≈ 0 (Fig. 10f). For $M = 1.0$ to $M = 3.0$, the amplitude of waves increases regressively. There is also a leftward shift of the waves (Fig. 10g and h). For $M = 10$, the amplitude again decreases a lot and there is also the formation of bolus for higher-valued waves (Fig. 10i). On increasing the Nb from 0.1 to 0.5, then to 1.0, there is a leftward shift of waves. For $Nb = 0.5$, the amplitude of the leftward waves remains almost unchanged, but for the rightward waves, the amplitude increases (Fig. 10j and k). For $Nb = 1.0$, the amplitude again increases for the right waves, and the amplitude decreases for the left waves. The gap between the waves also increases as we move toward the higher waves (Fig. 10l). A similar effect is seen for Nt also. For $Nt = 0.5$ to 1.5 to 2.5, the amplitude increases for the rightward waves, and the amplitude decreases for the leftward waves (Fig. 10m and n). A significant left shift is seen in the waves for higher waves (Fig. 10o).

5.8. Concentration contours

Fig. 11 shows the fluid concentration plots for different physical parameters The concentration waves are just lateral inversions of the temperature waves. For $M = 2.0$ to $M = 6.0$, the amplitude of the concentration waves increases drastically. There is also the formation of boluses between all the waves (Fig. 11a and b). For $M = 9.0$, the bolus size increase and the between layers merge (Fig. 11c). For $Nb = 0.1$ to 0.5, the amplitude of all the waves increases, however, there is a lesser change in the rightward waves (Fig. 11d and e). For $Nb = 1.0$, the amplitude increases heavily. There is also the formation of boluses on the left waves. The waves are
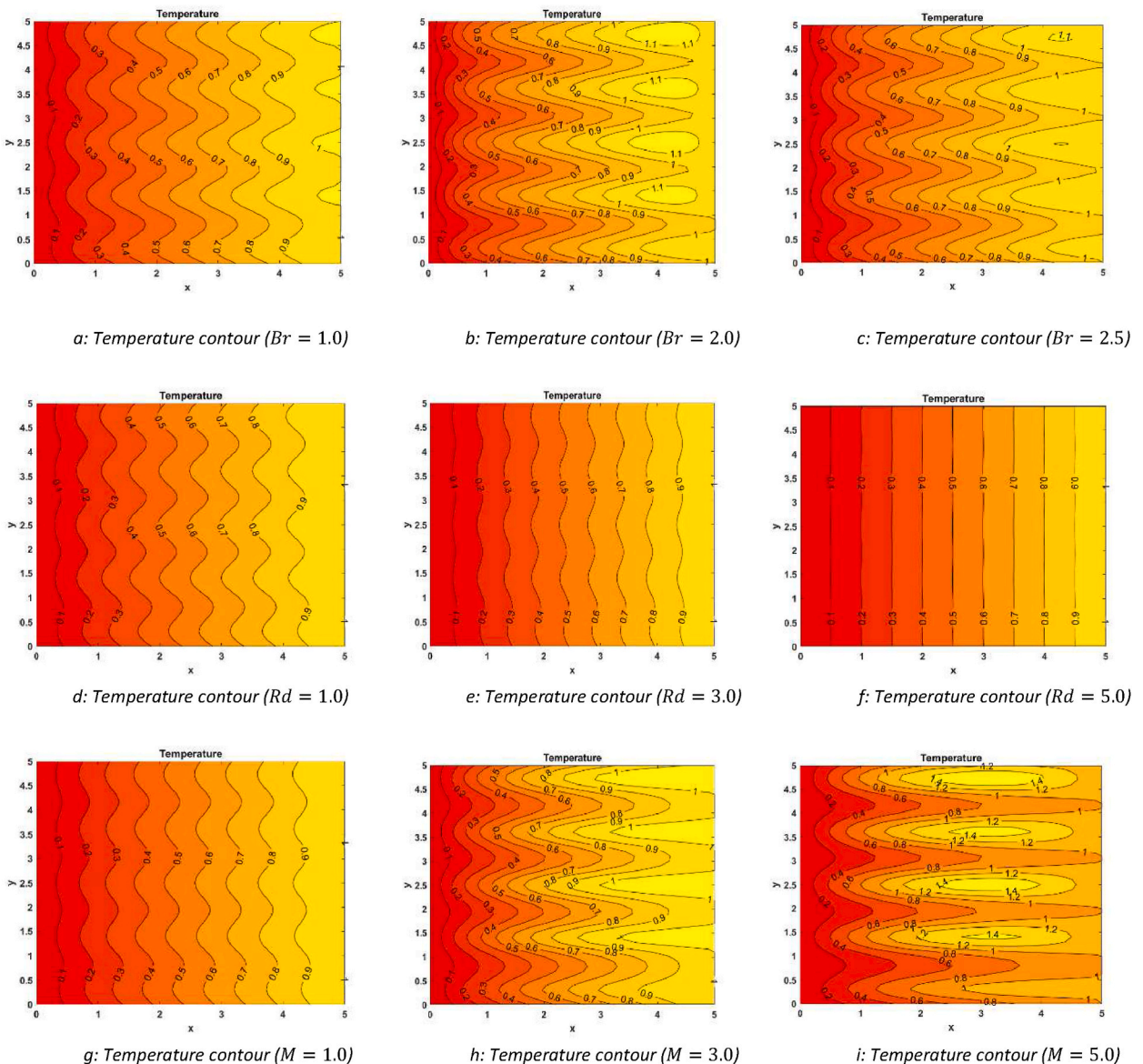

a: Temperature contour ($Br = 1.0$)

b: Temperature contour ($Br = 2.0$)

c: Temperature contour ($Br = 2.5$)

d: Temperature contour ($Rd = 1.0$)

e: Temperature contour ($Rd = 3.0$)

f: Temperature contour ($Rd = 5.0$)

g: Temperature contour ($M = 1.0$)

h: Temperature contour ($M = 3.0$)

i: Temperature contour ($M = 5.0$)

Fig. 10. Temperature contours.

j: Temperature contour (Nb = 0.1)

k: Temperature contour (Nb = 0.2)

l: Temperature contour (Nb = 0.3)

m: Temperature contour (Nt = 0.1)

n: Temperature contour (Nt = 0.2)

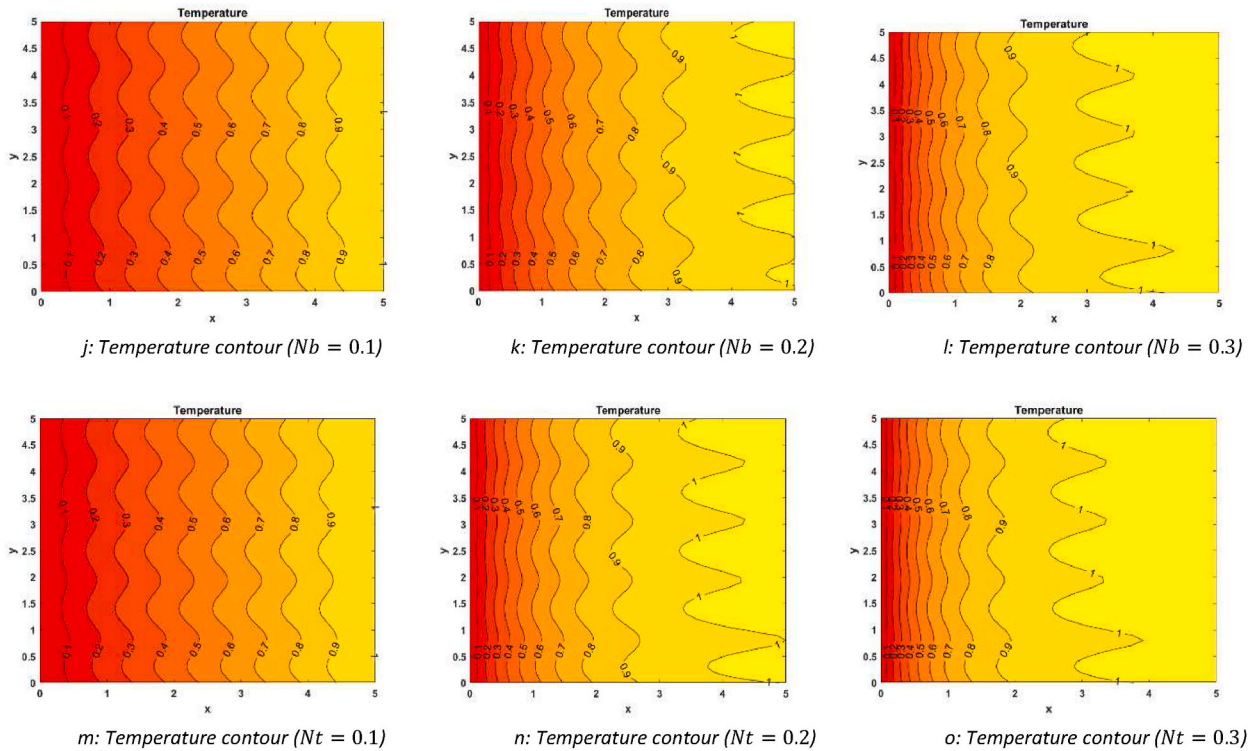o: Temperature contour (Nt = 0.3)

Fig. 10. (*continued*).

seen to have horizontal stretching (Fig. 11f). For $Nt = 0.5$ to $Nt = 1.5$ (Fig. 11g and h), there is a formation of boluses to the left side of the plot. The amplitude also increases for the smaller waves. For $Nt = 2.5$, The boluses disappear, and the amplitudes again increase significantly. There is also a leftward shift of the waves (Fig. 11i). For $Kr_1 = 0.1$ to 1.0, the formation of boluses starts on the left side. There is also an increase in amplitude for the lower waves (Fig. 11j and k). For $Kr_1 = 2.0$, the formation of boluses gets bigger. The amplitude of waves also decreased (Fig. 11l). For $Sc = 1.0$ to $Sc = 2.5$, the amplitude increases for the left waves and the wavelength is seen to be decreasing for the rightward waves. There is also a right shift of waves (Fig. 11m and n). For $Sc = 5.0$, the right shift increased, and the bolus formation starts for the lower waves (as seen in Fig. 11o).

5.9. Microorganisms density contours

Fig. 12 shows the microorganism's density contours for different physical parameters. Like the temperature and concentration, vertical waves are formed here. For $\Gamma = 0.1$ to 0.5, there is an increase in the amplitude of waves. There is also a bolus formation on the plot's left side (Fig. 12a and b). For $\Gamma = 1.0$, the size of boluses is increasing. There is also one layer formed around the boluses and minor change is seen in the higher-valued waves (Fig. 12c). For $M = 1.0$ to $M = 2.5$, an increment in the wave amplitude is seen. There is also a rightward shift of the waves (Fig. 12d and e). Again, for the 5.0 value, the amplitude is enhanced. However, the gap between the waves remains the same in all three cases (Fig. 12f). For $Pe = 0.1$ to $Pe = 0.5$, there is a formation of boluses on the left side of the waves. A drastic rightward shift can be seen in the figure. There are few changes for the higher waves (Fig. 12g and h). For $Pe = 1.0$, the density plots see a left shift of waves. There is also a formation of a bigger bolus outside the bolus formed in the case of $Pe = 0.5$ (Fig. 12i).

5.10. Electroosmosis contours

Fig. 13 shows the electroosmosis contours for different physical parameters. There is a symmetric effect seen with reference to the zero line ($x = 0$). The waves are the same as discussed for the earlier dimensionless quantities. For changing $K = 1.5$ to $K = 2.5$, the left waves move to the left side, and the right waves move toward the right direction. The waves move away from the zero line (Fig. 13a and b). For $K = 3.5$, again, the same effect happens but in an emerging way. The waves move away from the zero line to a greater extent (Fig. 13c). For $\zeta_1 = 0.025$ to $\zeta_1 = 0.050$ (Fig. 13d and e), there is the disappearing effect of the right waves. The gap of left side waves increases a lot. The magnitude decreases on moving toward the left side. For $\zeta_1 = 0.075$, there is again the same effect repeats itself. The amplitude of the waves increases for the lower waves. Then the amplitude decreases as we move toward the left side (as shown in Fig. 13f). Next, we discuss the ζ_2. For $\zeta_2 = 0.025$ to $\zeta_2 = 0.050$, again, the disappearing effect happens. But in contrast to the ζ_1, it happens for the left waves. For the right waves, the amplitude increases first for the higher waves (Fig. 13g and h), then it

decreases for the lower waves (having negative values). Then for $\zeta_2 = 0.075$, The amplitude of the zero-line waves increases, and then the amplitude decreases for the right-side waves. There is also a wavy effect for the zero line itself (Fig. 13i).

5.11. Physical significance quantities

Fig. 14 shows the physical interest quantities for various fluid numbers of non-dimensional ODEs obtained in this study. Fig. 14a illustrates the skin friction contour plot for the thermal Grashof and electroosmotic numbers. By enhancing the thermal Grashof number, the skin friction coefficient decreases. For increased values of the electroosmotic parameter, the skin friction increased. Fig. 14b conveys the skin friction contour plot for Darcy and magnetic numbers. According to the figure, by increasing the Darcy number, the skin friction coefficient decreases. For enhanced magnetic numbers, the skin friction coefficient increases. Fig. 14c depicts the radiation and Brinkman numbers' Nusselt number or the heat transfer rate. It shows that on increasing the radiation number, the Nusselt number increases in the negative direction. For enhanced values of the Brinkman number, the Nusselt number again increases in the negative magnitude. Fig. 14d reveals the Nusselt number contour plot for the Darcy and magnetic numbers. By growing the Darcy number, the Nusselt number's negative values boost up. On raising the magnetic number, the Nusselt number again starts increasing on the negative side. Fig. 14e indicates the Sherwood number or mass transfer rate contour plots for Brownian motion and Thermophoresis numbers. For escalated values of the Brownian motion number, the Sherwood number reduces. For larger values of the thermophoresis parameter, the Sherwood number enhances. Fig. 14f illustrates the Sherwood number contour plot for the Schmidt
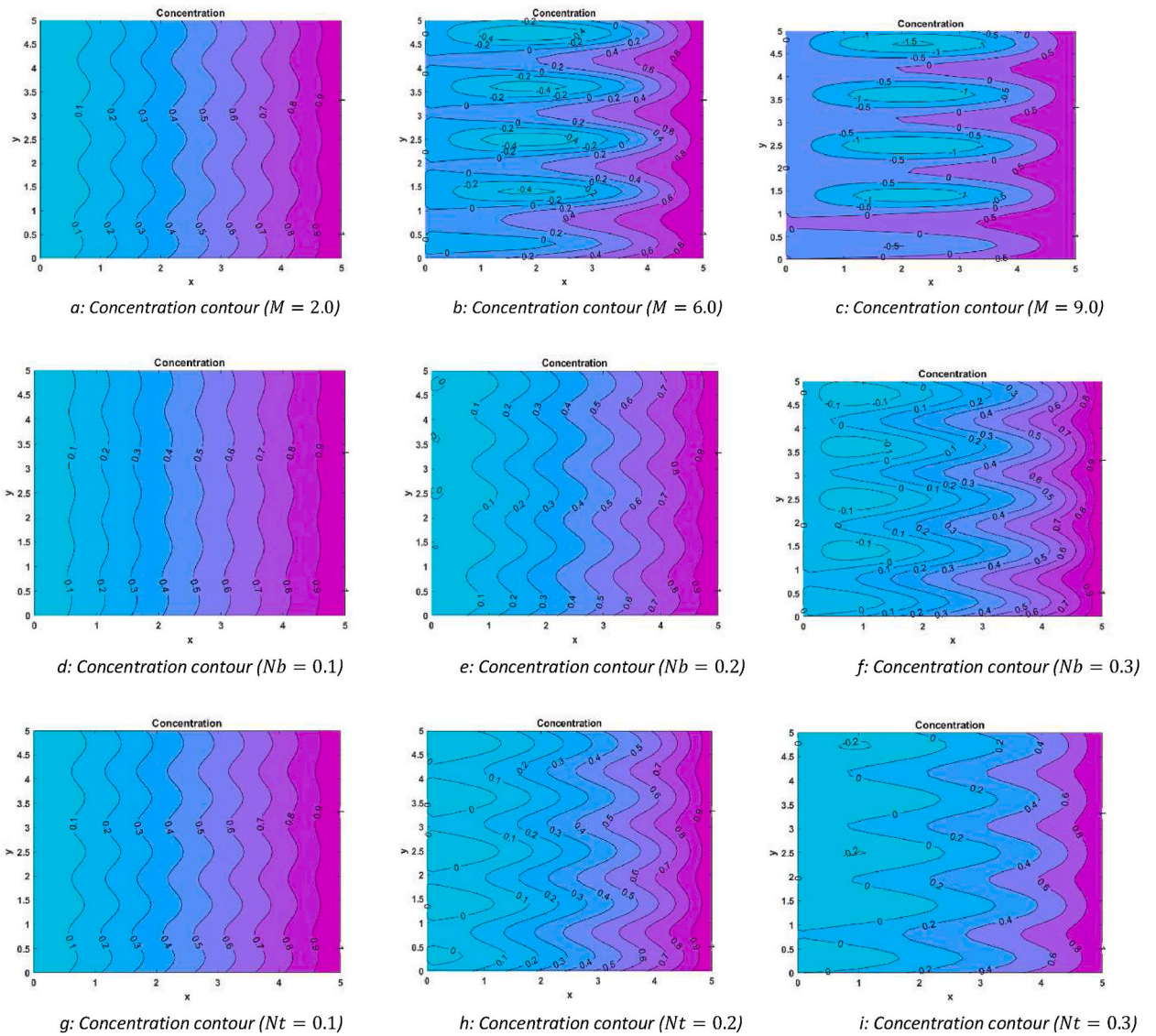

a: Concentration contour ($M = 2.0$)   b: Concentration contour ($M = 6.0$)   c: Concentration contour ($M = 9.0$)

d: Concentration contour ($Nb = 0.1$)   e: Concentration contour ($Nb = 0.2$)   f: Concentration contour ($Nb = 0.3$)

g: Concentration contour ($Nt = 0.1$)   h: Concentration contour ($Nt = 0.2$)   i: Concentration contour ($Nt = 0.3$)

Fig. 11. Concentration contours.

j: Concentration contour ($Kr_1 = 0.1$)   *k: Concentration contour ($Kr_1 = 1.0$)*   *l: Concentration contour ($Kr_1 = 2.0$)*

m: Concentration contour ($Sc = 1.0$)   *n: Concentration contour ($Sc = 2.5$)*   *o: Concentration contour ($Sc = 5.0$)*
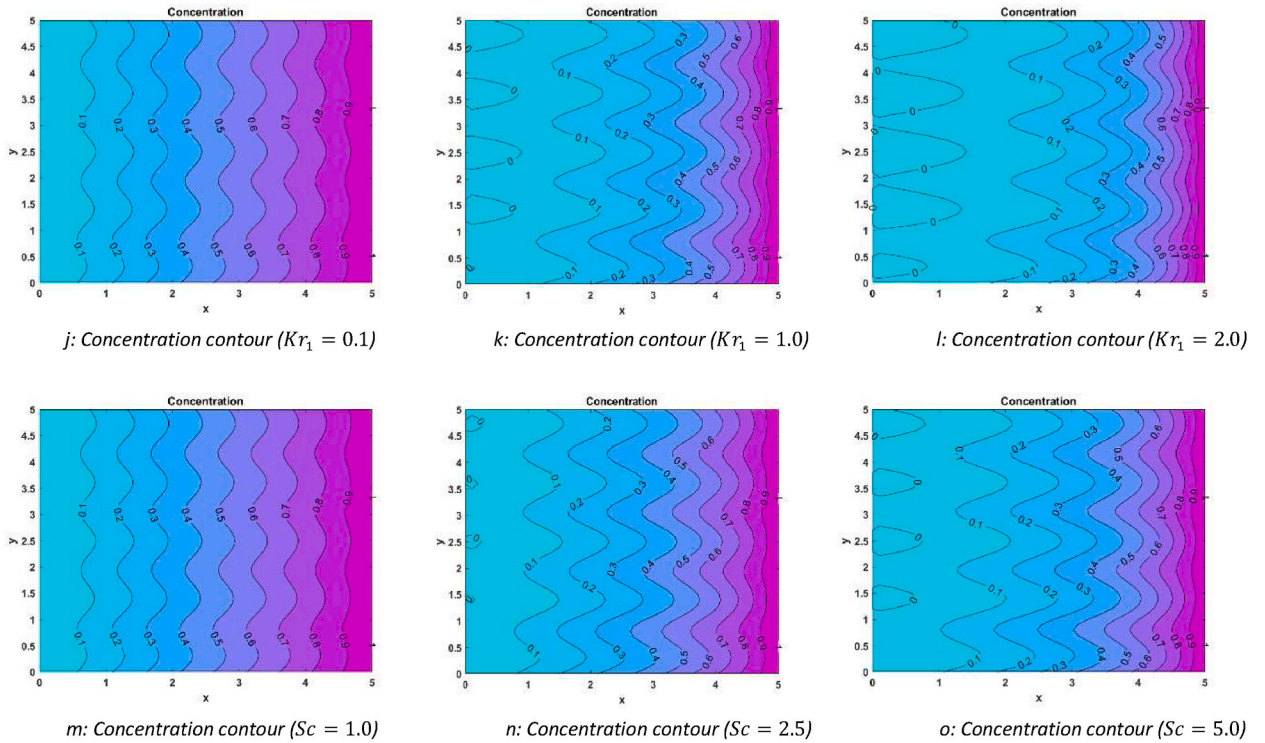
Fig. 11. (*continued*).

number and chemical reaction number. For increasing values of the Schmidt number and chemical reaction parameter the Sherwood number reduces. Fig. 14g shows the entropy generation contour plots for the Brinkman number and magnetic number. On increasing the Brinkman number, the entropy generation increases. For improved values of magnetic number, the entropy generation increases. The purpose of Fig. 14h is to show the entropy generation contour plot for the Darcy number and the radiation number. It is observed that by increasing the Darcy number, the entropy generation increases. For increasing values of the thermal radiation parameter, the entropy generation also increases. Fig. 14i depicts the Bejan number contour plot for the Brinkman number and magnetic number. For larger values of the Brinkman number and magnetic parameter, the Bejan number also boosts up. Fig. 14j shows the Bejan number contour plot for the Darcy number and the thermal radiation number. It is observed that as the Darcy number or radiation number increases, the Bejan number also increases.

6. Conclusion

With PVA serving as the base fluid, this study examines the ternary hybrid nanofluid, which combines the effects of viscous dissipation, thermal radiation, Brownian motion, electroosmotic, porous media, magnetic field, and nanoparticles of gold (Au) and silver (Ag). The following are visually explained with appropriate justifications: velocity, temperature, concentration, density of microorganisms, electroosmosis profiles, heat transfer rate (Nusselt number), mass transfer rate (Sherwood number), skin friction coefficient, entropy production, and Bejan number. The following are the study's key findings:

- The velocity profiles increase for increasing the Darcy number while reverse effect is noticed for magnetic parameter.
- The temperature profiles increase for an increase in magnetic parameter, Darcy parameter, Brinkman number, radiation parameter and decrease with respect to gold concentration, time-average flow rate constant.
- The microorganism density profiles increase for reduced microorganism density ratio and Peclet number.
- The skin friction increases for a decline of thermal Grashof parameter, Darcy parameter and enhancement is observed for electroosmotic parameter and magnetic parameter.
- The heat transfer rate increase for an increase in radiation, magnetic, Brinkman, and Darcy numbers.
- The mass transfer rate increases for boosted thermophoretic number while, reverse effect is observed for Brownian motion number, Schmidt number, and chemical reaction number.
- The entropy generated in the fluid increases by increasing the radiation, magnetic, Brinkman, and Darcy parameter.
- The Bejan number enhances for increasing radiation, magnetic, Brinkman, and Darcy parameters.

The research holds significant potential for real-life applications. The insights gained could pave the way for designing advanced
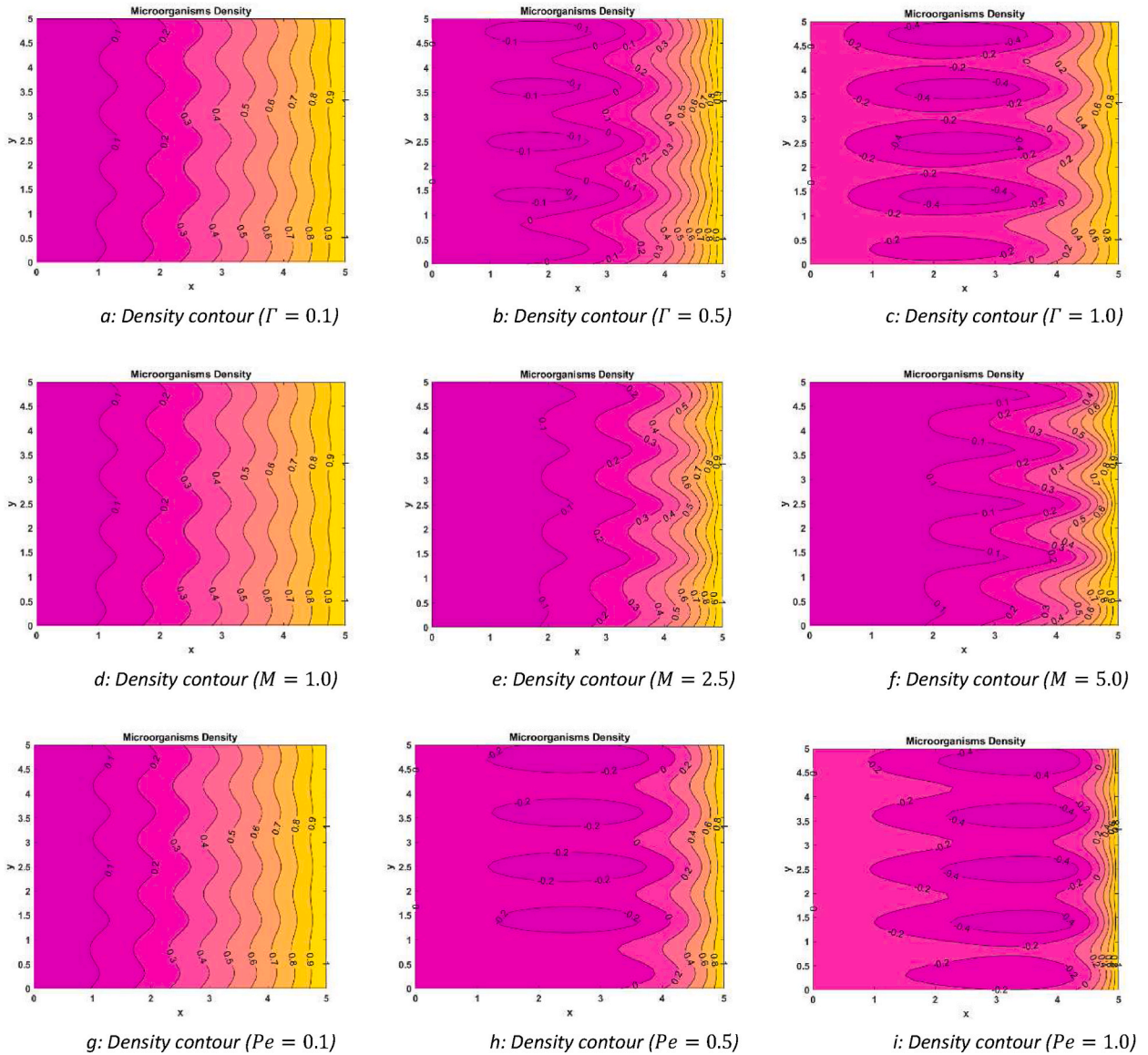
a: Density contour ($\Gamma = 0.1$)   b: Density contour ($\Gamma = 0.5$)   c: Density contour ($\Gamma = 1.0$)

d: Density contour ($M = 1.0$)   e: Density contour ($M = 2.5$)   f: Density contour ($M = 5.0$)

g: Density contour ($Pe = 0.1$)   h: Density contour ($Pe = 0.5$)   i: Density contour ($Pe = 1.0$)

Fig. 12. Microorganisms density contours.

microfluidic devices for efficient energy harvesting, lab-on-a-chip technologies, and targeted drug delivery systems. Additionally, the understanding of gyrotactic microorganism behavior within the flow regime could find practical utility in environmental remediation, bioremediation, and bioprocess optimization, fostering innovation in sustainable biotechnological solutions. Disadvantages of this study may include simplified model assumptions and idealized material properties. These limitations can be addressed in the future by incorporating more realistic parameters and refining the model. The development of this research could involve advanced microorganism modeling, experimental validation, and exploring external factors' impact. Mathematical complexities and experimental constraints might arise, requiring robust interdisciplinary collaboration for solutions.

7. Limitations

The present study has provided valuable insights into the complex interactions within the investigated system. However, some limitations should be acknowledged to ensure a comprehensive understanding of the study's scope and implications.

1. **Simplifications in Model:** The complexity of the physical system necessitates some simplifications in the mathematical model. These simplifications might overlook certain real-world intricacies, potentially affecting the accuracy of predictions.
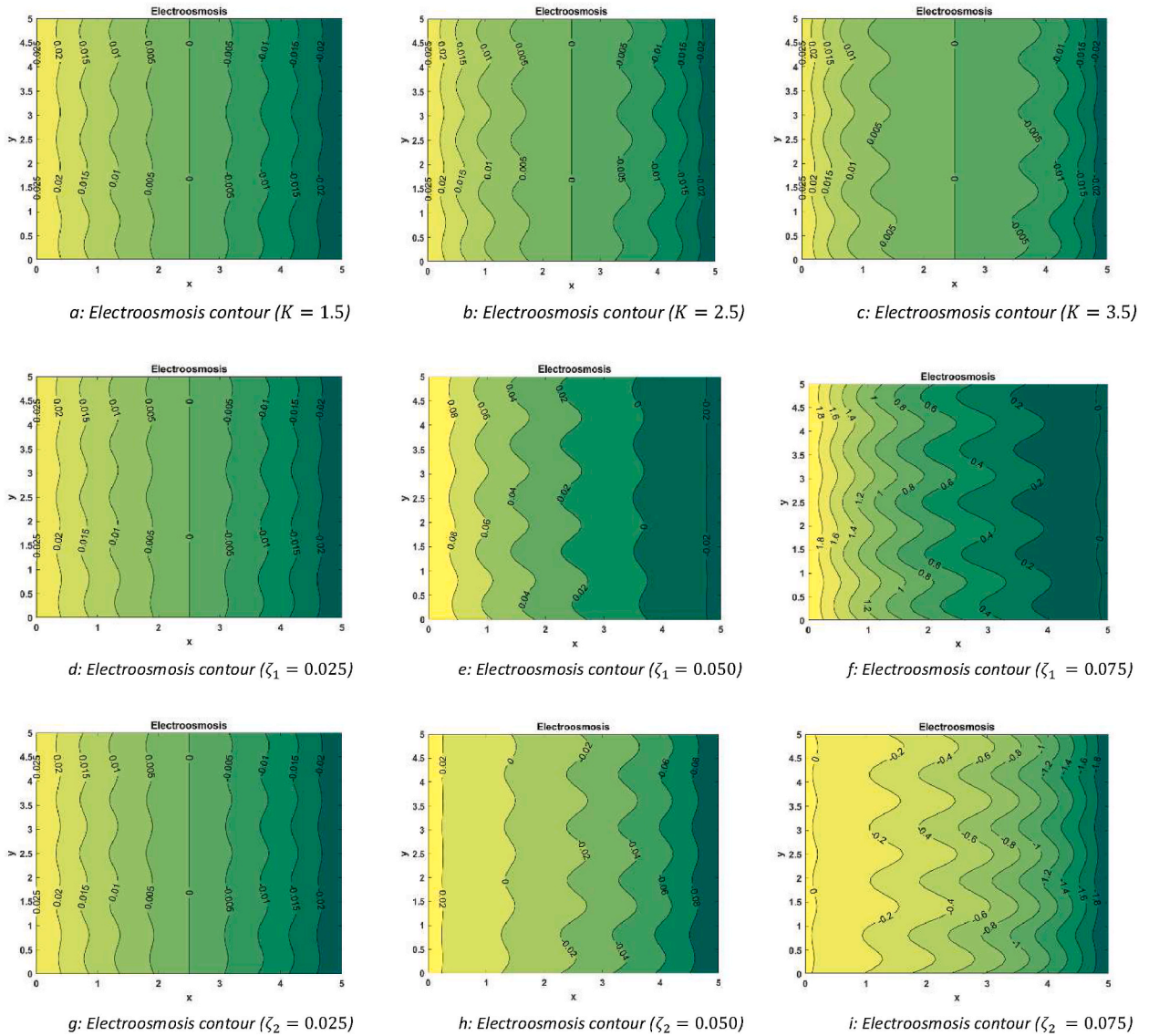
a: Electroosmosis contour ($K = 1.5$)   b: Electroosmosis contour ($K = 2.5$)   c: Electroosmosis contour ($K = 3.5$)

d: Electroosmosis contour ($\zeta_1 = 0.025$)   e: Electroosmosis contour ($\zeta_1 = 0.050$)   f: Electroosmosis contour ($\zeta_1 = 0.075$)

g: Electroosmosis contour ($\zeta_2 = 0.025$)   h: Electroosmosis contour ($\zeta_2 = 0.050$)   i: Electroosmosis contour ($\zeta_2 = 0.075$)

Fig. 13. Electroosmosis contours.

2. **Material Properties:** The study likely assumes ideal material properties for nanofluids and microorganisms. In reality, the properties can vary significantly, and considering more realistic values could enhance the validity of the findings.

3. **Boundary Conditions:** The chosen boundary conditions may not fully capture the intricacies of interactions between nanofluids, microorganisms, and the ciliated channel walls. These conditions could affect the accuracy of the predictions in complex flow scenarios.

4. **Microorganism Behavior:** The model's assumption of ideal gyrotactic microorganism behavior might not fully reflect the complexities of their responses to fluid dynamics. More refined models could incorporate additional factors that influence microorganism movement and concentration.

8. Future scope

The following are potential directions for extending and enhancing the understanding of the investigated system:

1. **Enhanced Nanofluid Characterization:** Investigate a broader range of nanofluid properties, including varying particle sizes, shapes, and concentrations, to better capture real-world behavior and interactions with the fluid flow.

2. **Refined Microorganism Modeling:** Develop an advanced gyrotactic microorganism model that incorporates more intricate behaviors and responses to fluid dynamics, potentially accounting for individual swimming strategies and interaction dynamics.

3. **Experimental Validation:** Conduct physical experiments within similar setups to validate the theoretical predictions, strengthening the credibility of the study's outcomes and bridging the gap between simulation and reality.
4. **External Factors Impact:** Investigate how external factors like external fields, biochemical reactions, and surface interactions influence nanofluid behavior and microorganism dynamics, enhancing the realism and accuracy of the model. Further, a stability analysis can be done to study the stability of problem due to various physical effects.

a: C_f vs K vs Gr

b: C_f vs M vs Da

c: Nu vs Rd vs Br

d: Nu vs M vs Da

e: Sh vs Nt vs Nb

f: Sh vs Kr_1 vs Sc

Fig. 14. Physical significance quantities.

g: EG vs M vs Br

h: EG vs Rd vs Da

i: Be vs M vs Br

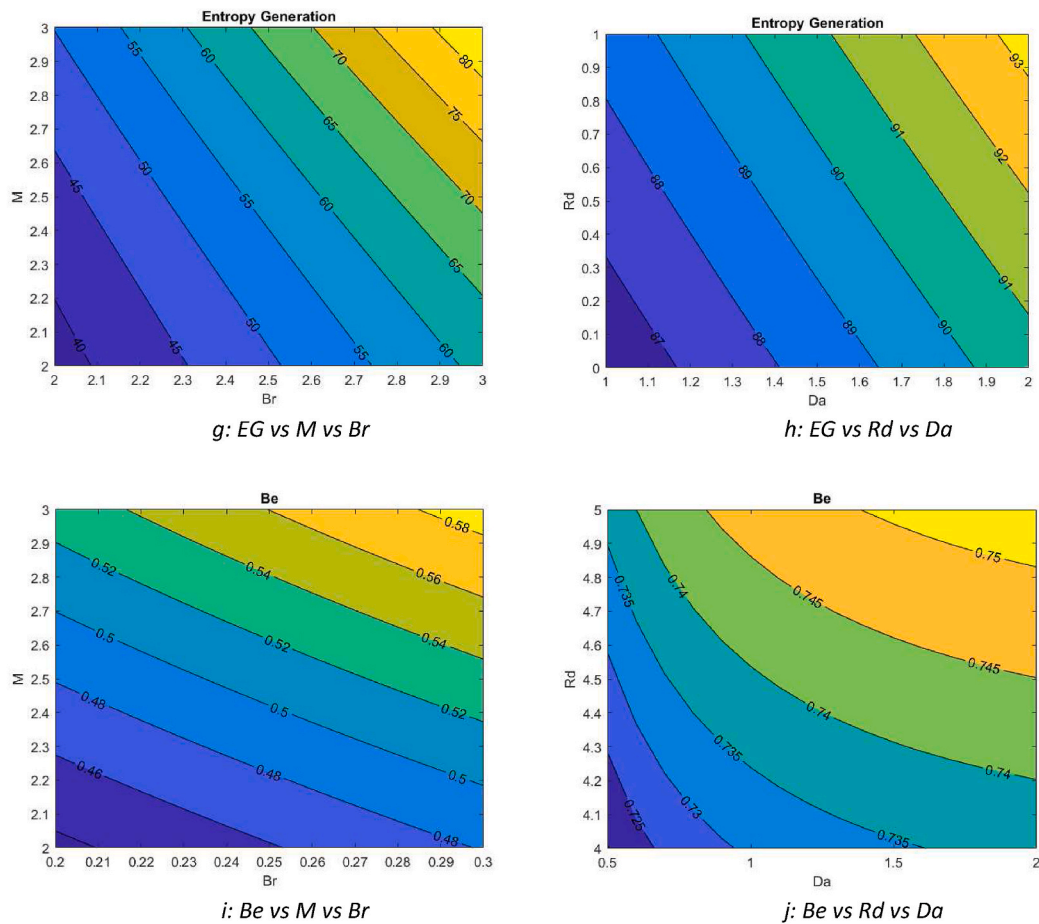j: Be vs Rd vs Da
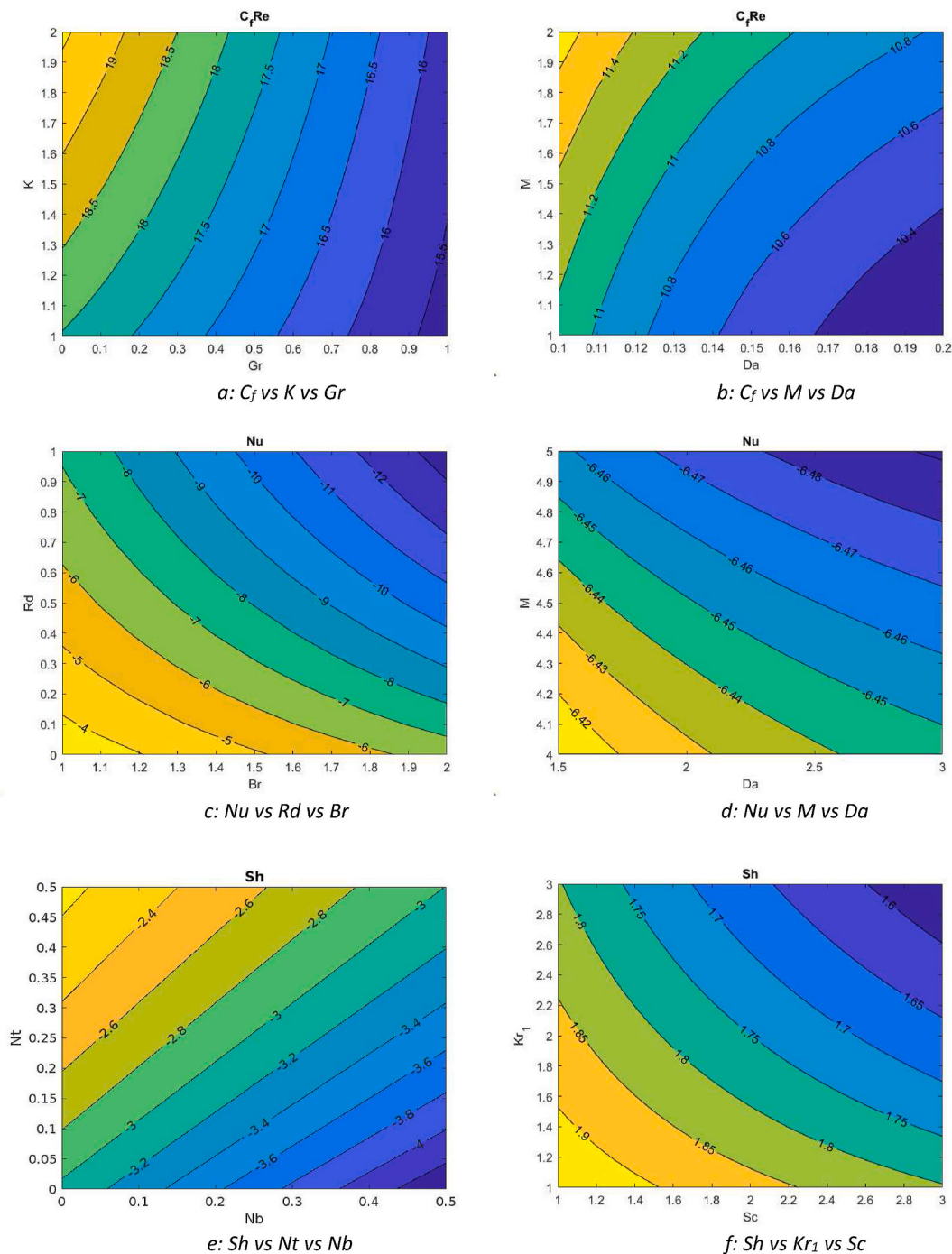
Fig. 14. (*continued*).

Data availability statement

All the data included in the article itself.

CRediT authorship contribution statement

Nidhish K. Mishra: Writing – original draft, Investigation, Conceptualization. **Parikshit Sharma:** Software, Methodology, Formal analysis. **Bhupendra K. Sharma:** Writing – original draft, Validation, Methodology, Conceptualization. **Bandar Almohsen:** Writing – review & editing, Supervision, Investigation. **Laura M. Pérez:** Writing – review & editing, Software, Methodology, Funding acquisition.

Declaration of competing interest

The authors declare that they have no known competing financial interests or personal relationships that could have appeared to influence the work reported in this paper.

References

[1] Y.X. Li, M.I. Khan, R.P. Gowda, A. Ali, S. Farooq, Y.M. Chu, S.U. Khan, Dynamics of aluminum oxide and copper hybrid nanofluid in nonlinear mixed Marangoni convective flow with entropy generation: applications to renewable energy, Chin. J. Phys. 73 (2021) 275–287.

[2] R.J. Punith Gowda, I.E. Sarris, R. Naveen Kumar, R. Kumar, B.C. Prasannakumara, A three-dimensional non-Newtonian magnetic fluid flow induced due to stretching of the flat surface with chemical reaction, J. Heat Tran. 144 (11) (2022) 113602.

[3] L.T. Benos, E.G. Karvelas, I.E. Sarris, Crucial effect of aggregations in CNT-water nanofluid magnetohydrodynamic natural convection, Therm. Sci. Eng. Prog. 11 (2019) 263–271.

[4] J.K. Madhukesh, I.E. Sarris, B.C. Prasannakumara, A. Abdulrahman, Investigation of thermal performance of ternary hybrid nanofluid flow in a permeable inclined cylinder/plate, Energies 16 (6) (2023) 2630.

[5] K. Sarada, F. Gamaoun, A. Abdulrahman, S.O. Paramesh, R. Kumar, G.D. Prasanna, R.P. Gowda, Impact of exponential form of internal heat generation on water-based ternary hybrid nanofluid flow by capitalizing non-Fourier heat flux model, Case Stud. Therm. Eng. 38 (2022) 102332.

[6] A.M. Jyothi, R.N. Kumar, R.P. Gowda, B.C. Prasannakumara, Significance of Stefan blowing effect on flow and heat transfer of Casson nanofluid over a moving thin needle, Commun. Theor. Phys. 73 (9) (2021) 095005.

[7] A. Alhadhrami, H.A. Alzahrani, R.N. Kumar, R.P. Gowda, K. Sarada, B.M. Prasanna, N. Madhukeshwara, Impact of thermophoretic particle deposition on Glauert wall jet slip flow of nanofluid, Case Stud. Therm. Eng. 28 (2021) 101404.

[8] F. Wang, S.P. Rani, K. Sarada, R.P. Gowda, H.Y. Zahran, E.E. Mahmoud, The effects of nanoparticle aggregation and radiation on the flow of nanofluid between the gap of a disk and cone, Case Stud. Therm. Eng. 33 (2022) 101930.

[9] M.D. Alsulami, A. Abdulrahman, R.N. Kumar, R.J. Punith Gowda, B.C. Prasannakumara, Three-dimensional swirling flow of nanofluid with nanoparticle aggregation kinematics using modified krieger–dougherty and maxwell–bruggeman models: a finite element solution, Mathematics 11 (9) (2023) 2081.

[10] M.D. Alsulami, R. Naveen Kumar, R.J. Punith Gowda, B.C. Prasannakumara, Analysis of heat transfer using Local thermal non-equilibrium conditions for a non-Newtonian fluid flow containing Ti6Al4V and AA7075 nanoparticles in a porous media, ZAMM-Journal of Applied Mathematics and Mechanics/Zeitschrift für Angewandte Mathematik und Mechanik 103 (5) (2023) e202100360.

[11] M.D. Alsulami, M.C. Jayaprakash, J.K. Madhukesh, G. Sowmya, R.N. Kumar, Bioconvection in radiative Glauert wall jet flow of nanofluid: a Buongiorno model, Waves Random Complex Media (2022) 1–18.

[12] B.R. Sreenivasa, J. Faqeeh A, A. Alsaiari, H.A. Alzahrani, M.Y. Malik, Numerical study of heat transfer mechanism in the flow of ferromagnetic hybrid nanofluid over a stretching cylinder, Waves Random Complex Media (2022) 1–17.

[13] W. Jamshed, R.J.P. Gowda, R.N. Kumar, B.C. Prasannakumara, K.S. Nisar, O. Mahmoud, A.A. Pasha, Entropy production simulation of second-grade magnetic nanomaterials flowing across an expanding surface with viscidness dissipative flux, Nanotechnol. Rev. 11 (1) (2022) 2814–2826.

[14] N. Elboughdiri, C.S. Reddy, A. Alshehri, S.M. Eldin, T. Muhammad, A. Wakif, A passive control approach for simulating thermally enhanced Jeffery nanofluid flows nearby a sucked impermeable surface subjected to buoyancy and Lorentz forces, Case Stud. Therm. Eng. (2023) 103106.

[15] K. Zhang, N.A. Shah, M. Alshehri, S. Alkarni, A. Wakif, S.M. Eldin, Water thermal enhancement in a porous medium via a suspension of hybrid nanoparticles: MHD mixed convective Falkner's-Skan flow case study, Case Stud. Therm. Eng. 47 (2023) 103062.

[16] G. Rasool, A. Shafiq, X. Wang, A.J. Chamkha, A. Wakif, Numerical treatment of MHD Al2O3–Cu/engine oil-based nanofluid flow in a Darcy–Forchheimer medium: application of radiative heat and mass transfer laws, Int. J. Mod. Phys. B (2023) 2450129.

[17] J. Sharma, N.A. Ahammad, A. Wakif, N.A. Shah, J.D. Chung, W. Weera, Solutal effects on thermal sensitivity of casson nanofluids with comparative investigations on Newtonian (water) and non-Newtonian (blood) base liquids, Alex. Eng. J. 71 (2023) 387–400.

[18] N. Elboughdiri, D. Ghernaout, T. Muhammad, A. Alshehri, R. Sadat, M.R. Ali, A. Wakif, Towards a novel EMHD dissipative stagnation point flow model for radiating copper-based ethylene glycol nanofluids: an unsteady two-dimensional homogeneous second-grade flow case study, Case Stud. Therm. Eng. 45 (2023) 102914.

[19] A. Wakif, Numerical inspection of two-dimensional MHD mixed bioconvective flows of radiating Maxwell nanofluids nearby a convectively heated vertical surface, Waves Random Complex Media (2023) 1–22.

[20] G. Rasool, A. Wakif, X. Wang, A. Shafiq, A.J. Chamkha, Numerical passive control of alumina nanoparticles in purely aquatic medium featuring EMHD driven non-Darcian nanofluid flow over convective Riga surface, Alex. Eng. J. 68 (2023) 747–762.

[21] A. Wakif, A. Abderrahmane, K. Guedri, B. Bouallegue, R. Kaewthongrach, P. Kaewmesri, A. Jirawattanapanit, Importance of exponentially falling variability in heat generation on chemically reactive von kármán nanofluid flows subjected to a radial magnetic field and controlled locally by zero mass flux and convective heating conditions: a differential quadrature analysis, Frontiers in Physics 10 (2022) 988275.

[22] B.K. Sharma, P. Sharma, N.K. Mishra, S. Noeiaghdam, U. Fernandez-Gamiz, Bayesian regularization networks for micropolar ternary hybrid nanofluid flow of blood with homogeneous and heterogeneous reactions: entropy generation optimization, Alex. Eng. J. 77 (2023) 127–148.

[23] B.K. Sharma, P. Sharma, N.K. Mishra, U. Fernandez-Gamiz, Darcy-Forchheimer hybrid nanofluid flow over the rotating Riga disk in the presence of chemical reaction: artificial neural network approach, Alex. Eng. J. 76 (2023) 101–130.

[24] D. Tripathi, J. Prakash, M.G. Reddy, J.C. Misra, Numerical simulation of double diffusive convection and electroosmosis during peristaltic transport of a micropolar nanofluid on an asymmetric microchannel, J. Therm. Anal. Calorim. 143 (2021) 2499–2514.

[25] S. Sikiru, T.L. Oladosu, S.Y. Kolawole, L.A. Mubarak, H. Soleimani, L.O. Afolabi, A.O.O. Toyin, Advance and prospect of carbon quantum dots synthesis for energy conversion and storage application: a comprehensive review, J. Energy Storage 60 (2023) 106556.

[26] B. Souayeh, K. Ali Abro, S. Bhattacharyya, Editorial for the special issue "heat transfer enhancement and fluid flow features due to the addition of nanoparticles in engineering applications", Energies 16 (5) (2023) 2228.

[27] D. Wang, M.A. Ali, K. Sharma, S.F. Almojil, A.A. Alizadeh, A.F. Alali, A.I. Almohana, Multiphase numerical simulation of exergy loss and thermo-hydraulic behavior with environmental cosiderations of a hybrid nanofluid in a shell-and-tube heat exchanger with twisted tape, Eng. Anal. Bound. Elem. 147 (2023) 1–10.

[28] A. Hashim, F.L. Rashid, M.H. Abbas, B.H. Rabee, Preparation of nanofluids from inorganic nanostructures doped PEG: characteristics and energy storage applications, East European Journal of Physics (1) (2023) 185–188.

[29] N. Fatima, K. Alayyash, W.F. Alfwzan, N. Ijaz, A. Riaz, N. Saleem, E.M.T. El-Din, Mathematical Model for Numerical Simulations of Thermal Energy of Nano-Fluid in a Complex Peristaltic Transport within a Curved Passage: Pharmacological and Engineering Biomedical Application, Case Studies in Thermal Engineering, 2023 102897.

[30] M.U. Sajid, Y. Bicer, Experimental Investigation of Spectrum Selective Nanofluids for Thermal Management of Greenhouses in Hot Arid Climates, Applied Thermal Engineering, 2023 120019.

[31] A.M. Abd-Alla, E.N. Thabet, F.S. Bayones, Numerical solution for MHD peristaltic transport in an inclined nanofluid symmetric channel with porous medium, Sci. Rep. 12 (1) (2022) 3348.

[32] A.J. Chamkha, On laminar hydromagnetic mixed convection flow in a vertical channel with symmetric and asymmetric wall heating conditions, Int. J. Heat Mass Tran. 45 (12) (2002) 2509–2525.

[33] A.J. Chamkha, T. Groşan, I. Pop, Fully developed free convection of a micropolar fluid in a vertical channel, Int. Commun. Heat Mass Tran. 29 (8) (2002) 1119–1127.

[34] J.C. Umavathi, A.J. Chamkha, A. Mateen, A. Al-Mudhaf, Unsteady two-fluid flow and heat transfer in a horizontal channel, Heat Mass Tran. 42 (2) (2005) 81–90.

[35] A.J. Chamkha, Unsteady laminar hydromagnetic fluid–particle flow and heat transfer in channels and circular pipes, Int. J. Heat Fluid Flow 21 (6) (2000) 740–746.

[36] J.P. Kumar, J.C. Umavathi, A.J. Chamkha, I. Pop, Fully-developed free-convective flow of micropolar and viscous fluids in a vertical channel, Appl. Math. Model. 34 (5) (2010) 1175–1186.

[37] S. Izadi, T. Armaghani, R. Ghasemiasl, A.J. Chamkha, M. Molana, A comprehensive review on mixed convection of nanofluids in various shapes of enclosures, Powder Technol. 343 (2019) 880–907.

[38] B. Kumar, G.S. Seth, R. Nandkeolyar, A.J. Chamkha, Outlining the impact of induced magnetic field and thermal radiation on magneto-convection flow of dissipative fluid, Int. J. Therm. Sci. 146 (2019) 106101.

[39] M.V. Krishna, N.A. Ahammad, A.J. Chamkha, Radiative MHD flow of Casson hybrid nanofluid over an infinite exponentially accelerated vertical porous surface, Case Stud. Therm. Eng. 27 (2021) 101229.

[40] M.V. Krishna, A.J. Chamkha, Hall and ion slip effects on unsteady MHD convective rotating flow of nanofluids—application in biomedical engineering, Journal of the Egyptian Mathematical Society 28 (1) (2020) 1.

[41] M.V. Krishna, B.V. Swarnalathamma, A.J. Chamkha, Investigations of Soret, Joule and Hall effects on MHD rotating mixed convective flow past an infinite vertical porous plate, J. Ocean Eng. Sci. 4 (3) (2019) 263–275.

[42] M.V. Krishna, A.J. Chamkha, Hall effects on MHD squeezing flow of a water-based nanofluid between two parallel disks, J. Porous Media 22 (2) (2019).

[43] A.J. Chamkha, MHD-free convection from a vertical plate embedded in a thermally stratified porous medium with Hall effects, Appl. Math. Model. 21 (10) (1997) 603–609.

[44] K. Javid, R. Khan, K. Al-Khaled, M.I. Khan, S.U. Khan, K. Guedri, A.M. Galal, EMHD ciliated pumping of viscoelastic liquid in a complex convergent/divergent channel, Waves Random Complex Media (2022) 1–23.

[45] A. Alsaedi, M.I. Khan, M. Farooq, N. Gull, T. Hayat, Magnetohydrodynamic (MHD) stratified bioconvective flow of nanofluid due to gyrotactic microorganisms, Adv. Powder Technol. 28 (1) (2017) 288–298.

[46] Y. Khan, S. Akram, M. Athar, K. Saeed, T. Muhammad, A. Hussain, H.A. Alsulaimani, The role of double-diffusion convection and induced magnetic field on peristaltic pumping of a Johnson–Segalman nanofluid in a non-uniform channel, Nanomaterials 12 (7) (2022) 1051.

[47] A. Kumar, A.K. Singh, Unsteady MHD free convective flow past a semi-infinite vertical wall with induced magnetic field, Appl. Math. Comput. 222 (2013) 462–471.

[48] B. Kumar, G.S. Seth, R. Nandkeolyar, A.J. Chamkha, Outlining the impact of induced magnetic field and thermal radiation on magneto-convection flow of dissipative fluid, Int. J. Therm. Sci. 146 (2019) 106101.

[49] M.K. Chaube, A. Yadav, D. Tripathi, Electroosmotically induced alterations in peristaltic microflows of power law fluids through physiological vessels, J. Braz. Soc. Mech. Sci. Eng. 40 (2018) 1–9.

[50] F. Ishtiaq, R. Ellahi, M.M. Bhatti, S.Z. Alamri, Insight in thermally radiative cilia-driven flow of electrically conducting non-Newtonian Jeffrey fluid under the influence of induced magnetic field, Mathematics 10 (12) (2022) 2007.

[51] A.S. Alnahdi, S. Nasir, T. Gul, Blood-based ternary hybrid nanofluid flow-through perforated capillary for the applications of drug delivery, Waves Random Complex Media (2022) 1–19.

[52] N.K. Mishra, M. Sharma, B.K. Sharma, U. Khanduri, Soret and Dufour effects on MHD nanofluid flow of blood through a stenosed artery with variable viscosity, Int. J. Mod. Phys. B (2023) 2350266.

[53] K. Ramesh, J. Prakash, Thermal analysis for heat transfer enhancement in electroosmosis-modulated peristaltic transport of Sutterby nanofluids in a microfluidic vessel, J. Therm. Anal. Calorim. 138 (2019) 1311–1326.

[54] K. Javid, U.F. Alqsair, M. Hassan, M.M. Bhatti, T. Ahmad, E. Bobescu, Cilia-assisted flow of viscoelastic fluid in a divergent channel under porosity effects, Biomech. Model. Mechanobiol. 20 (2021) 1399–1412.

[55] B.K. Sharma, U. Khanduri, N.K. Mishra, K.S. Mekheimer, Combined effect of thermophoresis and Brownian motion on MHD mixed convective flow over an inclined stretching surface with radiation and chemical reaction, Int. J. Mod. Phys. B (2022) 2350095.

[56] A. Tassaddiq, S. Khan, M. Bilal, T. Gul, S. Mukhtar, Z. Shah, E. Bonyah, Heat and mass transfer together with hybrid nanofluid flow over a rotating disk, AIP Adv. 10 (5) (2020) 055317.

[57] N. Saleem, S. Munawar, D. Tripathi, Entropy analysis in ciliary transport of radiated hybrid nanofluid in presence of electromagnetohydrodynamics and activation energy, Case Stud. Therm. Eng. 28 (2021) 101665.

[58] B.K. Sharma, C. Kumawat, O.D. Makinde, Hemodynamical analysis of MHD two phase blood flow through a curved permeable artery having variable viscosity with heat and mass transfer, Biomech. Model. Mechanobiol. 21 (3) (2022) 797–825.

[59] B.K. Sharma, Poonam, A.J. Chamkha, Effects of heat transfer, body acceleration and hybrid nanoparticles (Au–Al2O3) on MHD blood flow through a curved artery with stenosis and aneurysm using hematocrit-dependent viscosity, Waves Random Complex Media (2022) 1–31.

[60] B.K. Sharma, A. Kumar, R. Gandhi, M.M. Bhatti, N.K. Mishra, Entropy generation and thermal radiation analysis of EMHD jeffrey nanofluid flow: applications in solar energy, Nanomaterials 13 (3) (2023) 544.

[61] R. Gandhi, B.K. Sharma, N.K. Mishra, Q.M. Al-Mdallal, Computer simulations of EMHD casson nanofluid flow of blood through an irregular stenotic permeable artery: application of koo-kleinstreuer-Li correlations, Nanomaterials 13 (4) (2023) 652.

[62] R. Gandhi, B.K. Sharma, C. Kumawat, O.A. Bég, Modeling and analysis of magnetic hybrid nanoparticle (au-al 2 o 3/blood) based drug delivery through a bell-shaped occluded artery with joule heating, viscous dissipation and variable viscosity effects, in: Proceedings of the Institution of Mechanical Engineers, Part E: Journal of Process Mechanical Engineering, vol. 236, 2022, pp. 2024–2043, 5.

[63] B.K. Sharma, U. Khanduri, N.K. Mishra, A.J. Chamkha, Analysis of Arrhenius activation energy on magnetohydrodynamic gyrotactic microorganism flow through porous medium over an inclined stretching sheet with thermophoresis and Brownian motion, in: Proceedings of the Institution of Mechanical Engineers, Part E: Journal of Process Mechanical Engineering, 2022 09544089221128768.

[64] B.K. Sharma, R. Gandhi, Combined effects of Joule heating and non-uniform heat source/sink on unsteady MHD mixed convective flow over a vertical stretching surface embedded in a Darcy-Forchheimer porous medium, Propulsion and Power Research 11 (2) (2022) 276–292.

[65] N. Saleem, S. Munawar, Significance of synthetic cilia and Arrhenius energy on double diffusive stream of radiated hybrid nanofluid in microfluidic pump under ohmic heating: an entropic analysis, Coatings 11 (11) (2021) 1292.

[66] R. Gandhi, B.K. Sharma, N.K. Mishra, Q.M. Al-Mdallal, Computer simulations of EMHD casson nanofluid flow of blood through an irregular stenotic permeable artery: application of koo-kleinstreuer-Li correlations, Nanomaterials 13 (4) (2023) 652.

[67] B.K. Sharma, R. Gandhi, N.K. Mishra, Q.M. Al-Mdallal, Entropy generation minimization of higher-order endothermic/exothermic chemical reaction with activation energy on MHD mixed convective flow over a stretching surface, Sci. Rep. 12 (1) (2022) 17688.